ARTICLES
https://doi.org/10.1038/s42255-018-0001-z
nature metabolism

GIP regulates inflammation and body weight by restraining myeloid-cell-derived S100A8/A9

Fernanda Dana Mantelmacher[1,7], Isabel Zvibel[1,7], Keren Cohen[1], Alona Epshtein[1], Metsada Pasmanik-Chor[2], Thomas Vogl[3], Yael Kuperman[4], Shai Weiss[1], Daniel J. Drucker[5], Chen Varol[1,6*] and Sigal Fishman[1*]

Enteroendocrine cells relay energy-derived signals to immune cells to signal states of nutrient abundance and control immunometabolism. Emerging data suggest that the gut-derived nutrient-induced incretin glucose-dependent insulinotropic polypeptide (GIP) operates at the interface of metabolism and inflammation. Here we show that high-fat diet (HFD)-fed mice with immune cell-targeted GIP receptor (GIPR) deficiency exhibit greater weight gain, insulin resistance, hepatic steatosis and significant myelopoiesis concomitantly with impaired energy expenditure and inguinal white adipose tissue (WAT) beiging. Expression of the S100 calcium-binding protein S100A8 was increased in the WAT of mice with immune cell-targeted GIPR deficiency and co-deletion of GIPR and the heterodimer S100A8/A9 in immune cells ameliorated the aggravated metabolic and inflammatory phenotype following a HFD. Specific GIPR deletion in myeloid cells identified this lineage as the target of GIP effects. Furthermore, GIP directly downregulated S100A8 expression in adipose tissue macrophages. Collectively, our results identify a myeloid-GIPR-S100A8/A9 signalling axis coupling nutrient signals to the control of inflammation and adaptive thermogenesis.

The gastrointestinal tract is the largest endocrine organ in the body harbouring enteroendocrine cells (EECs) along its entirety. On sensing ingested nutrients and macromolecules, EECs secrete dozens of hormones, which act in an autocrine, paracrine and endocrine manner to regulate glucose homeostasis and energy balance[1]. Extensive evidence supports the physiological importance and therapeutic potential of different gut-derived peptides (GDPs) in the control of body weight[2]. Classic concepts highlight roles for GDPs in conveying the status of nutrient availability to the brain, initiating changes in eating behaviour and energy expenditure to maintain energy balance[1]. EEC hormones, such as glucagon-like peptide-1 (GLP-1), illustrate the therapeutic potential of understanding gut hormone interorgan cross-talk[2]. Although less well studied, multiple immune cell subsets express an extended repertoire of receptors for GDPs, suggesting incompletely understood immunoregulatory roles for gut hormones[3]. Given the growing comprehension of how innate and adaptive immune cell responses in adipose tissue regulate adipocyte function and metabolic homeostasis in health and disease[4], delineating the cellular and signalling networks that participate in linking GDPs to the immune and metabolic systems may have immediate translational relevance.

Evidence from rodent and in vitro models has indicated that the gut-derived incretin hormone GIP has anabolic effects by facilitating fat storage in adipocytes[5–7]. Later studies have suggested that GIP represents an important EEC peptide signalling state of nutrient abundance at the immunometabolism interface. Notably, in the setting of diet-induced obesity, augmentation of GIPR signalling by either genetically modified GIP overexpression[8] or by continuous administration of a degradation-resistant GIP analogue ([D-Ala^2]GIP)[9], attenuates adipose tissue infiltration of pro-inflammatory innate and adaptive immune cells. Given the multisystem properties of GIP and the diverse repertoire of cells expressing its receptor[10], the cells and mechanisms mediating GIP–immune cell interactions require careful elucidation.

Here we address the role of GIP in bone marrow (BM) myeloid cells. Our study reveals an original facet of GIPR-dependent regulation of energy homeostasis in obesity via myeloid cells and altered expression of the S100 calcium-binding protein heterodimer S100A8/A9.

Results

Aggravated diet-induced obesity and insulin resistance in *Gipr*$^{-/-}$ BM mice. GIPR is expressed in extra-pancreatic tissues, including hypothalamus and adipose tissues, thus controlling systemic metabolism beyond insulin secretion[11]. GIPR is also expressed on immune cells, such as monocytes[12,13] and macrophages[13–15], implying unexplored immunoregulatory properties for GIP. To investigate the physiological importance of GIPR in immune cells, we utilized a BM chimerism approach. The BM of lethally irradiated wild-type (WT) recipient mice was differentially reconstituted by transplantation of WT or *Gipr*$^{-/-}$ BM. Following immune cell reconstitution, mice were subjected to 14 weeks of a high-fat diet (HFD). After 6 weeks of HFD feeding, *Gipr*$^{-/-}$ BM mice displayed significantly increased weight gain compared with WT BM mice (Fig. 1a and Supplementary Fig. 1a) with similar average calorie consumption (Fig. 1b). Body weight increase was maintained in the *Gipr*$^{-/-}$ BM mice also after 18 weeks of a HFD (Supplementary Fig. 1d). There was no difference in body weight gain between these groups fed a regular chow diet (Supplementary Fig. 1b,c). *Gipr*$^{-/-}$ BM mice also exhibited higher epididymal WAT (epiWAT) mass, a reduced

[1]The Research Center for Digestive Tract and Liver Diseases, Tel-Aviv Sourasky Medical Center and the Sackler School of Medicine, Tel-Aviv University, Tel-Aviv, Israel. [2]Bioinformatics Unit, Faculty of Life Science, Tel Aviv University, Tel-Aviv, Israel. [3]Institute of Immunology, University of Münster, Münster, Germany. [4]Department of Veterinary Resources, Weizmann Institute of Science, Rehovot, Israel. [5]The Lunenfeld-Tanenbaum Research Institute, Mount Sinai Hospital, University of Toronto, Toronto, Ontario, Canada. [6]Department of Clinical Microbiology and Immunology, Sackler School of Medicine, Tel-Aviv University, Tel-Aviv, Israel. [7]These authors contributed equally: Fernanda Dana Mantelmacher, Isabel Zvibel. *e-mail: chenv@tlvmc.gov.il; sigalf@tlvmc.gov.il

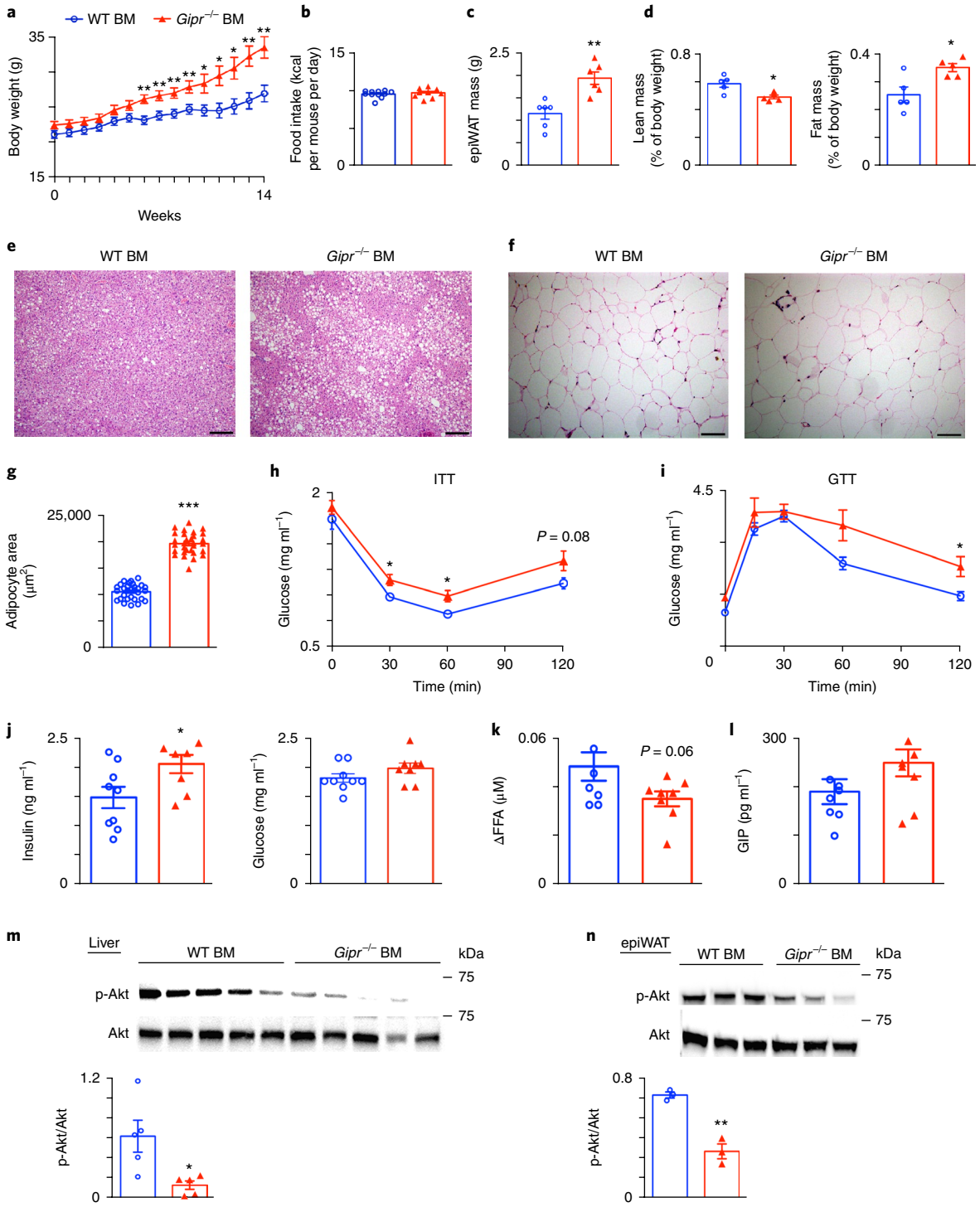

Fig. 1 | *Gipr*$^{-/-}$ BM mice display increased weight gain and insulin resistance. Mice were reconstituted with WT BM (blue open circles) or *Gipr*$^{-/-}$ BM (red triangles) for 6 weeks and then fed a HFD for 14 weeks. **a**, Weekly measurements of body weight (g) ($n=10$, time point week 0–14 $P=0.003$, $P=0.007$, $P=0.006$, $P=0.009$, $P=0.021$, $P=0.014$, $P=0.013$, $P=0.005$, $P=0.006$). **b**, Average food consumption during a period of 48 h ($n=11$). **c**, Average epiWAT mass ($n=6$, $P=0.001$). **d**, Computed tomography analysis of percentage of lean mass (left, $n=5$, $P=0.01$) and fat mass (right, $n=8$, $P=0.014$). **e**, Liver H&E paraffin sections. Original magnification, ×10. Scale bars, 200 μm. **f**, EpiWAT H&E paraffin. Original magnification, ×20. Scale bars, 100 μm. **g**, Average adipocyte area quantitated from 30 images taken from 3 distinct mice for each group ($P=0.0001$). **h**, Insulin tolerance test (ITT) showing before and following insulin injection (0.75 U per kg body weight) (for WT BM $n=6$, for *Gipr*$^{-/-}$ BM $n=5$, 30 min $P=0.034$, 1 h $P=0.014$). **i**, Glucose tolerance test (GTT) assessed by injecting 2 mg per g body weight glucose solution ($n=4$, $P=0.029$). **j**, ELISA measurement of fasting serum insulin levels (left, $n=9$, $P=0.032$) and glucose levels (right, $n=9$). **k**, Serum ΔFFA measurement by ELISA before and after insulin administration ($n=9$). **l**, ELISA measurements of serum GIP levels ($n=9$). **m**,**n**, Top: representative immunoblots of liver (**m**) and epiWAT (**n**) of total Akt and phosphorylated Akt (p-Akt). Mice were injected with insulin 30 min before being killed. Bottom: densitometry calculation showing the ratio of p-Akt/Akt in liver (**m**, $n=5$, $P=0.018$) and epiWAT (**n**, $n=3$, $P=0.002$). Data were analysed by unpaired, two-tailed *t*-test, comparing between WT BM and *Gipr*$^{-/-}$ BM mice. Data are presented as mean ± s.e.m with significance $^{*}P<0.05$, $^{**}P<0.01$ and $^{***}P<0.001$. Data in **a**–**c**, **e**–**g** and **l**–**m** are representative of three independent experiments, and data in **h**–**l** are from one experiment.

percentage of lean mass and an increased percentage of fat mass, greater liver steatosis, and adipocyte hypertrophy in both epiWAT and inguinal WAT (ingWAT) (Fig. 1c–g and Supplementary Fig. 1e). Expression of metabolic genes in liver and epiWAT was not significantly different between the groups (Supplementary Fig. 1f,g). Normal xylose absorption and comparable fat content in the faeces under regular chow and HFD conditions ruled out the possibility that the change in weight gain was secondary to differences in intestinal nutrient absorption (Supplementary Fig. 2a–c). *Gipr*$^{-/-}$ BM mice also exhibited impaired insulin and glucose tolerance (Fig. 1h,i and Supplementary Fig. 1i) and had significantly higher serum insulin concentrations with comparable glucose levels (Fig. 1j), consistent with insulin resistance. Moreover, serum free fatty acids (FFA) were reduced to a lesser extent by insulin in *Gipr*$^{-/-}$ BM mice (Fig. 1k), and circulating serum GIP levels were similar in WT versus *Gipr*$^{-/-}$ BM mice (Fig. 1l). Consistent with their defective insulin action, *Gipr*$^{-/-}$ BM mice exhibited reduced insulin-induced phosphorylation of protein kinase B (Akt) in both liver and epiWAT (Fig. 1m,n). These results emphasize that the selective impairment of GIPR signalling in BM-derived immune cells increases weight gain and deteriorates glucose homeostasis.

Increased myelopoiesis and S100A8 production in *Gipr*$^{-/-}$ BM mice. A large body of evidence has linked obesity with adipose tissue inflammation and insulin resistance[4]. We detected increased expression of Ly6C^{hi} monocyte and neutrophil recruitment chemokines *Ccl2* and *Cxcl1*, respectively, in the epiWAT of *Gipr*$^{-/-}$ BM mice (Fig. 2a). Moreover, epiWAT expression of the gene encoding the pro-inflammatory alarmin S100A8 (*S100a8*), representing one subunit of the heterodimer S100A8/A9, was increased, while the expression of other inflammatory cytokines was not affected (Fig. 2a). The same pattern of elevated *Ccl2*, *Cxcl1* and *S100a8* gene expression was also detected in the livers of *Gipr*$^{-/-}$ BM mice (Supplementary Fig. 3). Immunoblots demonstrated increased expression of S100A8 in epiWAT of *Gipr*$^{-/-}$ BM mice (Fig. 2b), though the serum level of the S100A8/A9 heterodimer was not different (Fig. 2c). Increased S100A8 expression in mice with diabetes or HFD-induced obesity has been mechanistically linked to BM myelopoiesis[16,17], and S100A8-driven recruitment of myeloid cells in HFD-fed mice precedes the development of metabolic symptoms[18]. Indeed, we observed increased representation of CD11b^{+} myeloid cells over CD11b^{-} lymphocytes in the blood and epiWAT of *Gipr*$^{-/-}$ BM mice (Fig. 2d,e). In the blood in particular, there was significant neutrophilia (Fig. 2d), and this was further mirrored in the epiWAT with increased representation of both neutrophils and Ly6C^{hi} monocytes (Fig. 2e). Overall myelopoiesis was further supported by a blood count showing elevation in the levels of platelets, erythrocytes, haemoglobin and haematocrit in *Gipr*$^{-/-}$ BM mice (Supplementary Fig. 4). Collectively, these results show that impaired GIPR signalling in BM-derived immune cells results in significant myelopoiesis, which may be driven by S100A8/A9.

Attenuated energy expenditure and beiging in *Gipr*$^{-/-}$ BM mice. *Gipr*$^{-/-}$ BM mice exhibited increased myelopoiesis and S100A8 production (Fig. 2). These mice also gained excessive weight, despite similar food intake (Fig. 1). To determine the underlying mechanisms, whole-body energy expenditure and food intake were simultaneously monitored in individually housed WT BM versus *Gipr*$^{-/-}$ BM mice over a 48-h period using automated caging systems. Mice were analysed at 8 weeks following the initiation of a HFD regimen, a time point when *Gipr*$^{-/-}$ BM mice display higher body weight gain versus WT BM mice (Fig. 1a). There was no difference in food intake between single-housed mice (Fig. 3a). Moreover, *Gipr*$^{-/-}$ BM mice displayed significantly reduced oxygen consumption and heat production (Fig. 3b,c), consistent with reduced energy expenditure. We next examined whether the effect of GIPR deletion in BM-derived cells on energy expenditure is attributable to reduced heat production in brown adipose tissue (BAT). Expression of uncoupling protein 1 (UCP1) and other thermogenesis-related genes was not different in BAT from the two groups (Supplementary Fig. 5a,b). However, adaptive thermogenesis also occurs in ingWAT during diet-induced obesity. Indeed, the reduced heat production in *Gipr*$^{-/-}$ BM mice was accompanied by reduced ingWAT gene expression of the transcription factor peroxisome proliferator-activated receptor-γ co-activator 1-α (PGC1α) (*Ppargc1a*) (Fig. 3d), known to increase both mitochondrial biogenesis and beiging[19]. UCP1 protein expression was also reduced in the ingWAT of *Gipr*$^{-/-}$ BM mice (Fig. 3e). The expression of mitochondrial respiration-associated genes was unchanged (Fig. 3d).

The increased inflammatory response, and especially S100A8/A9 production, may be linked to reduced energy expenditure in *Gipr*$^{-/-}$ BM mice. To assess whether S100A8/A9 modulates energy expenditure, mice were treated with vehicle (saline) or S100A8/A9 and were exposed to 24 h of cold challenge. Haematoxylin and eosin (H&E) staining and UCP1 immunohistochemistry revealed that S100A8/A9 reduced beiging in ingWAT (Fig. 3f). This was further corroborated by immunoblots displaying reduced expression of the beiging markers PGC1α and UCP1 in the ingWAT of S100A8/A9-treated mice (Fig. 3g). Therefore, increased S100A8/A9 disrupts cold-induced adaptive thermogenesis.

Immune S100A8/A9 drives metabolic phenotype of *Gipr*$^{-/-}$ BM mice. S100A8 is a key inducer of myeloid pro-inflammatory immune responses in epiWAT with deleterious metabolic implications[16–18]. S100A8 expression was significantly increased in the epiWAT of *Gipr*$^{-/-}$ BM mice concomitantly with significant myelopoiesis (Fig. 2). Therefore, the metabolic and immune phenotypes observed in the *Gipr*$^{-/-}$ BM mice may be mediated via increased S100A8/A9 production. To test this hypothesis, we reconstituted lethally irradiated mice with BM from *Gipr*$^{-/-}$*S100a9*$^{-/-}$ double knockout mice (*Gipr*$^{-/-}$/*S100a9*$^{-/-}$ BM). *S100a9*$^{-/-}$ mice were chosen given the embryonic lethality of *S100a8*$^{-/-}$ mice and since *S100a9*$^{-/-}$ mice do not express a mature S100A8 protein due to its high turnover in the absence of S100A9[20,21]. Notably, the profound increase in body weight gain and epiWAT mass witnessed in the *Gipr*$^{-/-}$ BM mice under a HFD was abolished in the *Gipr*$^{-/-}$/*S100a9*$^{-/-}$ BM mice (Fig. 4a,b), despite similar food intake (Fig. 4c). In addition, insulin sensitivity was similar between *Gipr*$^{-/-}$/*S100a9*$^{-/-}$ BM and WT BM mice (Fig. 4d). Moreover, the decreased gene expression of *Ucp1* and *Ppargc1a* in the ingWAT of *Gipr*$^{-/-}$ BM mice was restored in *Gipr*$^{-/-}$/*S100a9*$^{-/-}$ BM mice to the control level (Fig. 4e). The enhanced liver steatosis and hepatic triglyceride content detected in *Gipr*$^{-/-}$ BM mice were also abolished in the *Gipr*$^{-/-}$/*S100a9*$^{-/-}$ BM mice (Fig. 4f,g). Importantly, similar weight gain patterns were observed after 18 weeks of a HFD (Supplementary Fig. 6a). These results highlight a pivotal role for S100A8/A9 in transducing the metabolic phenotype arising in GIPR-deficient BM-derived immune cells following a HFD. Of note, the sole deletion of S100A8/A9 in immune cells (*S100a9*$^{-/-}$ BM) did not induce significant changes in most metabolic parameters, when compared with WT BM mice (Fig. 4a–g), suggesting that loss of basal BM-derived S100A8/A9 is insufficient, by itself, to trigger distinct metabolic phenotypes.

We next sought to define the consequences of an impaired GIPR–S100A8/A9 axis using microarray-based analysis of gene expression in epiWAT and ingWAT from WT BM, *Gipr*$^{-/-}$ BM and *Gipr*$^{-/-}$/*S100a9*$^{-/-}$ BM mice after a HFD. Principal component analysis (PCA) revealed a resemblance between the WT BM and *Gipr*$^{-/-}$/*S100a9*$^{-/-}$ BM groups, especially in the epiWAT (Fig. 4h). Hierarchical clustering of differentially expressed genes revealed distinct gene expression signatures in *Gipr*$^{-/-}$ BM and WT BM mice in both epiWAT and ingWAT, while the gene expression profile of *Gipr*$^{-/-}$/*S100a9*$^{-/-}$ BM mice clustered with that of the WT BM group

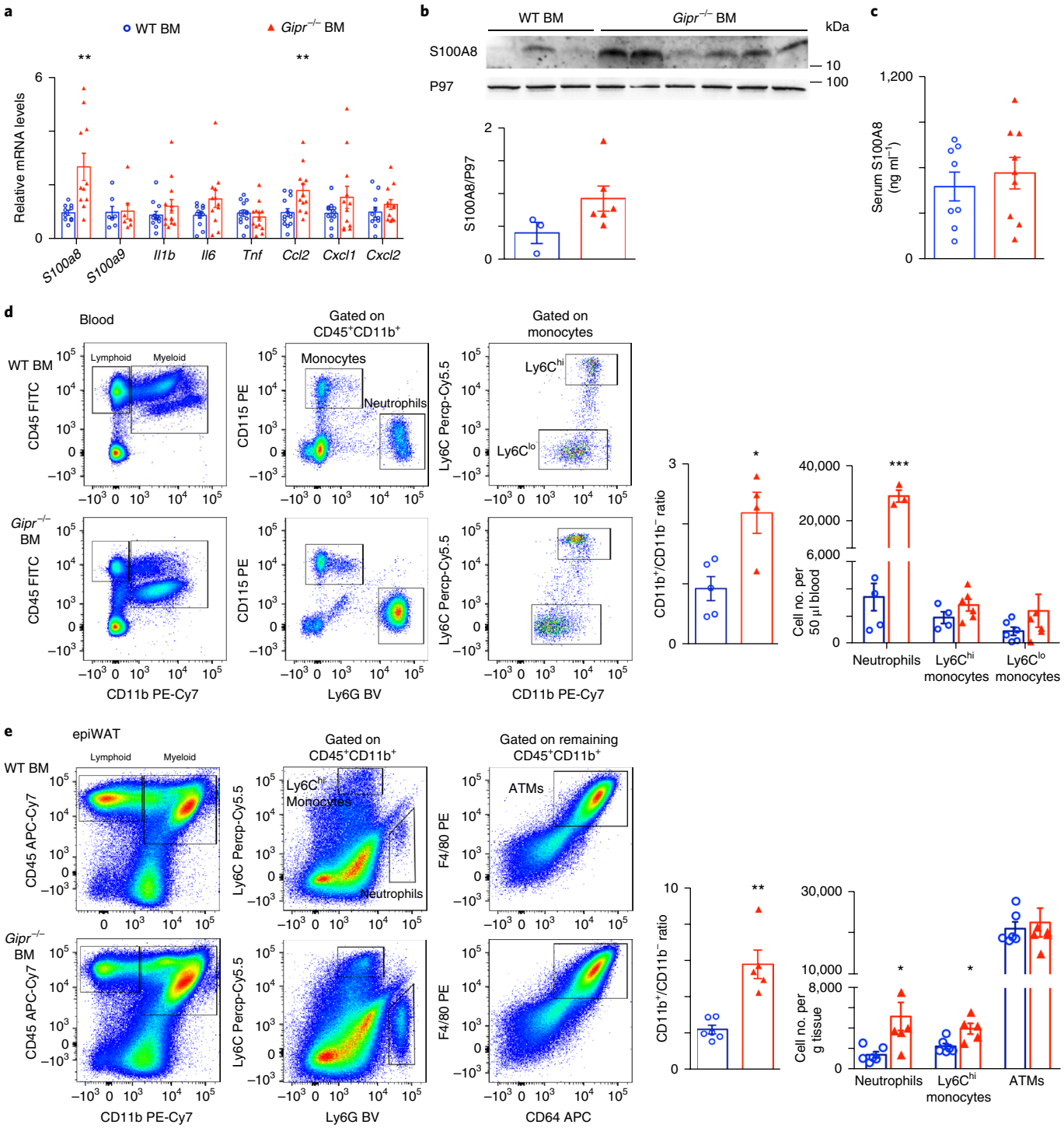

Fig. 2 | epiWAT of *Gipr*$^{-/-}$ BM mice shows increased expression of S100A8 and myelopoiesis. Mice were reconstituted with WT BM (blue open circles) or *Gipr*$^{-/-}$ BM (red triangles) for 6 weeks and then fed a HFD for 14 weeks. **a**, Expression of inflammatory mediators in epiWAT was determined by qRT-PCR analysis with normalization to *Rplp0* ($n=13$, for *S100a8* $P=0.005$, for *Ccl2* $P=0.006$). **b**, Representative immunoblots of epiWAT demonstrating protein expression and quantitation of S100A8. P97 was used as loading control ($n=3$ for WT BM, $n=6$ for *Gipr*$^{-/-}$ BM). **c**, S100A8/A9 levels in the serum were measured by ELISA ($n=10$). **d**,**e**, Left: representative flow cytometry images depicting the gating strategy for circulating (**d**) or epiWAT (**e**) myeloid immune cells. Middle right: graphs showing the ratio of CD11b^{+} phagocytes versus CD11b^{-} lymphocytes in the blood ($n=6$, $P=0.012$) (**d**) and epiWAT ($n=6$, $P=0.001$) (**e**), as an indication for myelopoiesis. Right: numbers of indicated myeloid cell populations per 50 µl of blood ($n=6$, $P<0.00001$) (**d**) or epiWAT mass g ($n=6$, for neutrophils $P=0.024$, for Ly6Chi monocytes $P=0.014$) (**e**). In the blood, CD45^{+}CD11b^{+}CD115^{+}Ly6G^{-} monocytes were dissected into Ly6C^{hi} and Ly6C^{lo} subsets, and neutrophils were defined as CD45^{+}CD11b^{+}CD115^{-}Ly6G^{hi} cells. In the epiWAT and ingWAT, adipose tissue macrophages (ATMs) were defined as CD45^{+}CD11b^{+}MHCII^{+}CD64^{+}F4/80^{+} cells; neutrophils as CD45^{+}CD11b^{+}MHCII^{-}CD64$^{-/lo}$F4/80$^{-/lo}$Ly6G^{hi} cells and Ly6C^{hi} monocytes as CD45^{+}CD11b^{+}MHCII^{-}CD64^{lo}F4/80^{lo}Ly6G^{-}Ly6C^{hi} cells. Data were analysed by an unpaired, two-tailed *t*-test, comparing between WT BM and *Gipr*$^{-/-}$ BM groups. Data are presented as mean ± s.e.m with significance $^{*}P<0.05$, $^{**}P<0.01$ and $^{***}P<0.001$. Data in **a** and **c**–**e** are representative of two independent experiments, and data in **b** are from one experiment.

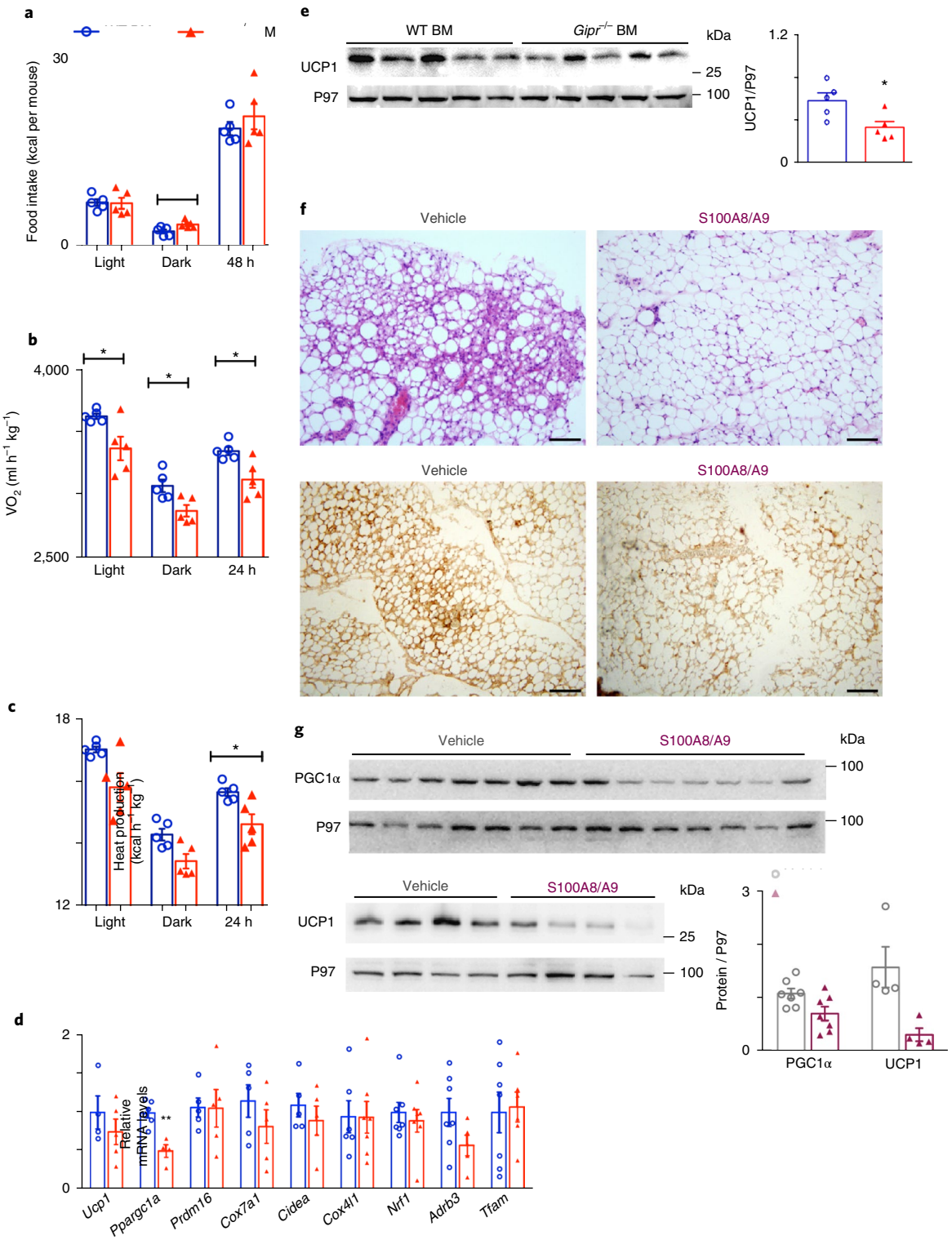

Fig. 3 | *Gipr*$^{-/-}$ BM mice exhibit attenuated energy expenditure. Mice were reconstituted with WT BM (blue open circles) or *Gipr*$^{-/-}$ BM (red triangles) for 6 weeks and then fed a HFD for 8 or 14 weeks. **a**–**c**, Mice were housed in metabolic cages (TSE Systems) for estimation of metabolic parameters in dark and light phase over a period of 48 h. Graphs show food intake ($n=5$, $P=0.028$) (**a**), oxygen consumption ($n=5$, for light, dark and 24 h $P=0.028$, $P=0.018$ and $P=0.015$) (**b**) and heat production ($n=5$, $P=0.016$) (**c**) of WT BM versus *Gipr*$^{-/-}$ BM mice after 8 weeks of HFD. **d**, Expression of thermogenesis genes in ingWAT after 14 weeks of a HFD as analysed by qRT-PCR and normalized to *Rplp0* ($n=7$, for *Ppargc1a* $P=0.0009$). **e**, UCP1 expression was assessed by immunoblot analysis and was quantified using P97 as loading control ($n=5$ for WT BM group, $n=5$ for *Gipr*$^{-/-}$ BM group, $P=0.024$). **f**, Representative images of H&E (top) and immunohistochemistry staining for UCP1 (bottom) in mice subjected to 24 h of cold challenge and pretreated with single injection of vehicle (saline) or 5 µg S100A8/A9. Original magnification, ×20. Scale bars, 100 µm. **g**, PGC1α and UCP1 expression was assessed by immunoblot analysis and was quantified using P97 as loading control ($n=7$ for PGC1α, $P=0.037$ and $n=4$ for UCP1, $P=0.019$). Data were analysed by unpaired, two-tailed *t*-test. Data are presented as mean ± s.e.m with significance $^{*}P<0.05$ $^{**}P<0.01$ and $^{***}P<0.001$. Data in **a**–**c** and **g** represent one experiment. Data in **d**–**f** represent two independent experiments.

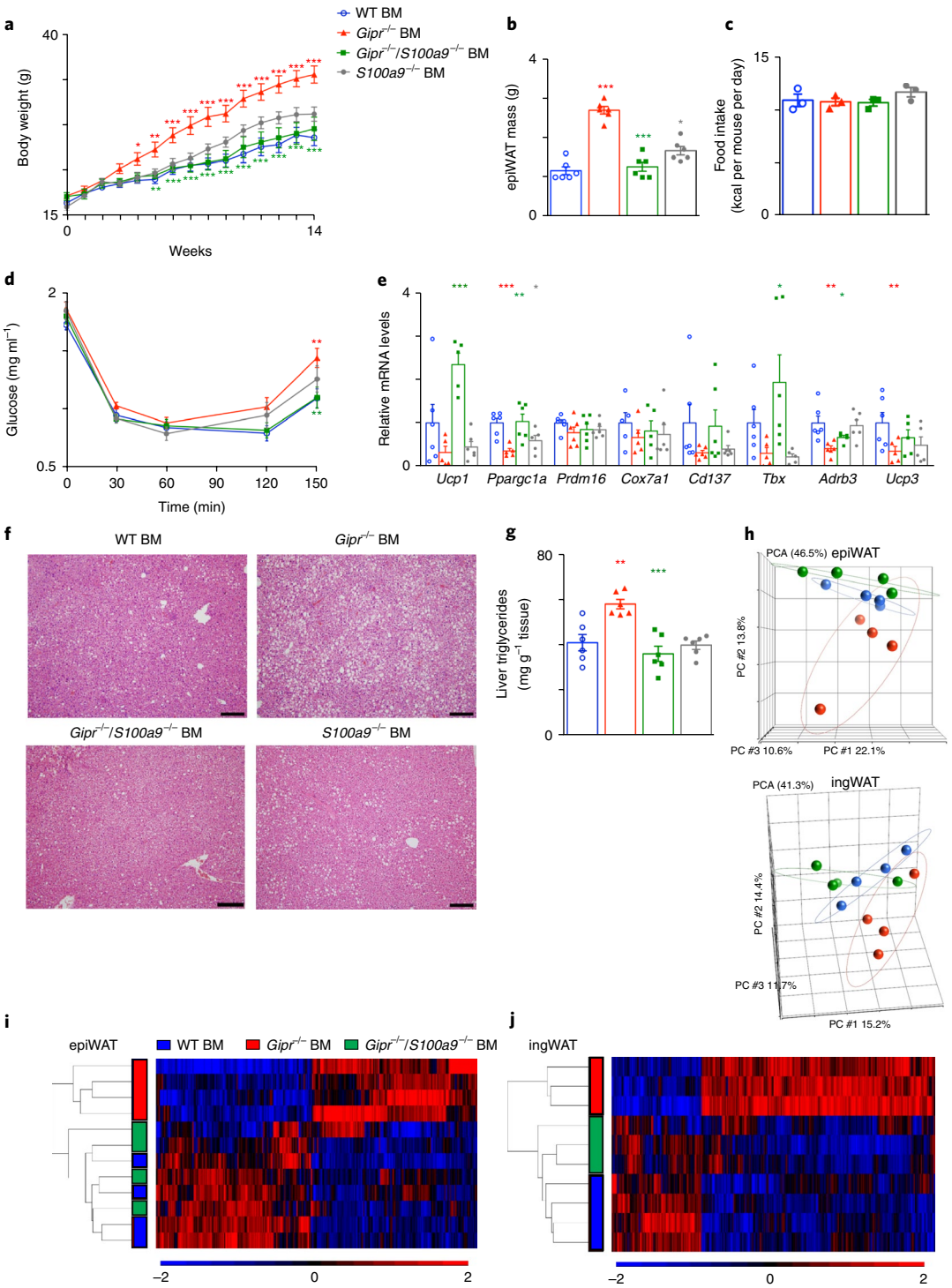

Fig. 4 | Double deletion of GIPR and S100A8/A9 from immune cells reverses the metabolic phenotype displayed by *Gipr*$^{-/-}$ BM mice. Mice were reconstituted with WT BM (blue open circles), *Gipr*$^{-/-}$ BM (red triangles), *Gipr*$^{-/-}$/*S100a9*$^{-/-}$ BM (green squares) and *S100a9*$^{-/-}$ BM (grey circles) for 6 weeks and then fed with a HFD for 14 weeks. **a**, Weekly measurements of body weight ($n=6$). **b**, Average epiWAT mass ($n=6$). **c**, Average food consumption during a period of 48 h, presented as kcal per mouse per day ($n=3$). **d**, Insulin sensitivity was estimated by ITT. Graph presents basal blood glucose levels and blood glucose following insulin injection (0.75 U per kg body weight) ($n=7$). **e**, qRT-PCR assessment of the expression of indicated thermogenesis genes in ingWAT normalized to *Rplp0* ($n=6$). **f**, Representative images of H&E liver paraffin sections for the assessment of hepatic steatosis. Original magnification, ×10. Scale bars, 200 µm. **g**, Liver triglyceride content (mg g^{-1} tissue) ($n=6$). **h**, 3D PCA plot showing the variance between groups in epiWAT and ingWAT ($n=4$). **i**,**j**, Hierarchical clustering of the differentially expressed genes (fold-change ≥ 2, $P<0.05$) performed on mRNA extracted from epiWAT (**i**) and ingWAT (**j**). A coloured bar indicating the standardized $\log_2$ intensities accompanies the expression profile. Data in **a** and **d** were analysed by two-way ANOVA with Bonferroni, and data in **b**, **c**, **e** and **g** were analysed by one-way ANOVA with Bonferroni. Data are presented as mean ± s.e.m. with significance $^*P<0.05$, $^{**}P<0.01$ and $^{***}P<0.001$. Red or grey stars represent significance of *Gipr*$^{-/-}$ BM or *S100a9*$^{-/-}$ BM groups versus WT BM, respectively. Green stars represent significance of *Gipr*$^{-/-}$/*S100a9*$^{-/-}$ BM versus *Gipr*$^{-/-}$ BM. Data in **a**–**c** represent two independent experiments, and data in **d**–**i** are from one experiment.

in both tissues (Fig. 4i,j). Further analysis revealed the same clustering pattern in specific metabolic pathways in both epiWAT and ingWAT (Supplementary Fig. 7a,b). Strikingly, 305 genes were differentially expressed between the WT BM and *Gipr*$^{-/-}$ BM groups; however, only 39 different genes remained differentially expressed between the WT and *Gipr*$^{-/-}$/*S100a9*$^{-/-}$ BM groups (Supplementary Fig. 7c). Therefore, these results support a pivotal role for S100A8/A9 in inducing the transcriptional changes observed in epiWAT and ingWAT of *Gipr*$^{-/-}$ BM versus WT BM mice.

Immune cell S100A8/A9 drives myelopoiesis in *Gipr*$^{-/-}$ BM mice. We next examined whether the impaired GIP–S100A8/A9 axis in immune cells contributes to the increased myelopoiesis observed in *Gipr*$^{-/-}$ BM mice (Fig. 2). Indeed, the increased myelopoiesis (CD11b^{+}/CD11b^{-} ratio) detected in the blood and epiWAT of *Gipr*$^{-/-}$ BM versus WT BM mice was completely diminished in *Gipr*$^{-/-}$/*S100a9*$^{-/-}$ BM mice (Fig. 5a). Importantly, recent studies have shown that inflammation in ingWAT impairs thermogenesis/beiging[22]. In line with this, there was increased myelopoiesis in ingWAT of *Gipr*$^{-/-}$ BM mice, which was strongly attenuated in the *Gipr*$^{-/-}$/*S100a9*$^{-/-}$ BM mice (Fig. 5a). Specifically, the significant neutrophilia observed in circulation and in the two WAT depots of *Gipr*$^{-/-}$ BM mice was abolished in the *Gipr*$^{-/-}$/*S100a9*$^{-/-}$ BM mice (Fig. 5b–d). Furthermore, the augmented infiltration of inflammatory Ly6C^{hi} monocytes in epiWAT and ingWAT of *Gipr*$^{-/-}$ BM mice was also attenuated in *Gipr*$^{-/-}$/*S100a9*$^{-/-}$ BM mice (Fig. 5c,d). Notably, the same pattern of immune cell distribution was also present after 18 weeks of a HFD (Supplementary Fig. 6b,c). Compatible with the augmented myeloid cell infiltration, *S100a8*, *Ccl2* and *Cxcl1* genes were significantly increased in epiWAT and ingWAT of *Gipr*$^{-/-}$ BM mice, but were similarly expressed between the WT BM and *Gipr*$^{-/-}$/*S100a9*$^{-/-}$ BM groups (Fig. 5e,f). *S100a9*$^{-/-}$ BM mice were comparable to WT BM mice in most parameters (Fig. 5). Further transcriptomic profiling of inflammatory pathways in epiWAT and ingWAT revealed the same consistent pattern of similarity between WT BM and *Gipr*$^{-/-}$/*S100a9*$^{-/-}$ BM mice as opposed to *Gipr*$^{-/-}$ BM mice (Supplementary Fig. 7a,b). Collectively, these results indicate that GIP plays an important immunoregulatory role in fat depot immune cells through its attenuation of S100A8/A9-driven inflammation.

***LysM*$^{\Delta Gipr}$ mice have severe metabolic and immune phenotype.** Myeloid cells, such as monocytes and neutrophils, are known to be the main producers of S100A8/A9[23]. Therefore, we hypothesized that GIP specifically restrains S100A8/A9 in myeloid cells. Flow cytometry analysis revealed that S100A8 is expressed by CD45^{+} immune cells in the epiWAT stromal vascular fraction (SVF) and non-parenchymal liver cells of *Gipr*$^{-/-}$ BM mice (Fig. 6a,b). S100A8 expression in these tissue fractions was restricted to ATMs and neutrophils, while Kupffer cells (KCs) were negative (Fig. 6a,b). GIPR gene expression was detected in epiWAT Ly6C^{hi} monocytes and ATMs after a HFD (Fig. 6c). Given the combined expression of GIPR and S100A8 by ATMs, we next examined the direct effect of GIP on S100A8 expression in ATMs sorted from HFD epiWAT (Supplementary Fig. 8). Indeed, [D-Ala^{2}]GIP treatment reduced *S100a8* expression in sorted ATMs (Fig. 6d). Moreover, mice treated with [D-Ala^{2}]GIP during the last 8 weeks of a 14 week HFD also exhibited reduced expression of *S100a8* in epiWAT ATMs (Fig. 6e). Of note, in both cases, [D-Ala^{2}]GIP treatment had no effect on ATM gene expression of the pro-inflammatory mediators interleukin-1 (IL-6; *Il6*), tumour-necrosis factor-α (*Tnf*) and IL-1β (*Il1b*) (Supplementary Fig. 9a,b), further underscoring the uniqueness of the GIP–S100A8/A9 axis in these cells. Lastly, we targeted GIPR deficiency to myeloid cells by crossing *Gipr*$^{fl/fl}$ mice[24] and Lyz2^{cre} mice (*LysM*$^{\Delta Gipr}$). After 14 weeks of a HFD, *LysM*$^{\Delta Gipr}$ mice exhibited higher body mass, despite similar food intake (13.5 ± 2.8 versus 13.9 ± 2.5 kcal per mouse per day), profound hepatic steatosis and impaired glucose tolerance (Fig. 6f–i), relative to littermate *Gipr*$^{fl/fl}$ controls. They also had increased myelopoiesis in the epiWAT (Fig. 6j,k), augmented *S100a8* expression in ingWAT and epiWAT (Fig. 6l), and decreased expression of the beiging-associated marker PGC1α in ingWAT at both transcriptional and protein levels (Fig. 6m,n). Collectively, these findings outline a pivotal immunoregulatory role for GIP in myeloid cell S100A8/A9-driven metabolic dysfunction and myelopoiesis.

Discussion

Herein we demonstrate a previously unappreciated role for the incretin hormone GIP in immune cells in the regulation of energy homeostasis and myelopoiesis under conditions of nutrient excess. GIPR deficiency in BM-derived cells impairs energy expenditure as manifested by reduced heat production and oxygen consumption and by impaired ingWAT beiging. This leads to weight gain and impaired insulin action. Moreover, *Gipr*$^{-/-}$ BM mice show profound myelopoiesis in the blood, epiWAT and ingWAT. We identify the myeloid lineage as a specific target of GIP regulation. Mechanistically, we show direct inhibition of S100A8 by GIP in ATMs. We also demonstrate that S100A8/A9 directly impairs cold-induced adaptive thermogenesis in ingWAT.

One of the most recognized extra-pancreatic effects of GIP is its anabolic effect on fat depots. Indeed, *Gipr*$^{-/-}$ mice exhibit resistance to weight gain and greater insulin sensitivity under conditions of prolonged nutrient excess[5]. In stark contrast, we report here that GIPR deficiency in myeloid cells unexpectedly leads to greater weight gain and insulin resistance. The question may be raised as to why GIPR deficiency in myeloid cells does not contribute to a deleterious metabolic and inflammatory role in the *Gipr*$^{-/-}$ mice. A possible explanation may be that in the absence of obesity-induced inflammation in these lean mice, resident fat depot immune cells (especially ATMs) are reduced in number and do not become inflammatory and other myeloid immune cells, such as neutrophils and Ly6C^{hi} monocytes, are not recruited. Our results uncover cell-specific roles for GIP in the context of dietary energy excess leading to obesity.

Consistent with cell-specific roles for GIPR signalling, a recent study demonstrated that selective GIPR inactivation in cardiomyocytes unexpectedly improves survival and reduces adverse cardiac muscle remodelling after experimental myocardial infarction, whereas GIPR agonism alone had little effect on cardiac outcomes[25]. Taken together, these studies underscore the importance of defining cell-specific actions of basal GIPR signalling to reveal its diverse physiological roles and understand its therapeutic potential.

The heterodimeric protein alarmin S100A8/A9, which is demonstrated in the current study to be modulated by GIP, belongs to a family of Ca^{++} binding proteins and is considered an important mediator and biomarker in various inflammatory disorders[20,23]. S100A8/A9 is mainly found in the cytoplasm of monocytes and neutrophils and locally released at sites of inflammation in a variety of different diseases[26]. The significant neutrophilia and monocytosis in both epiWAT and ingWAT of *Gipr*$^{-/-}$ BM and flow cytometry intracellular staining for S100A8 in neutrophils and ATMs suggest that these cells are the likely sources for the prominent increase in S100A8 expression within these tissues. Several studies have demonstrated that elevated visceral adipose tissue and serum expression of S100A8 is an early marker in type 2 diabetes mellitus (T2DM)[27], as well as a novel marker for obesity[28] that is reduced following bariatric surgery[29]. In line with our results, S100A8/A9 is mainly expressed by cells within the SVF in adipose tissue of obese subjects, and its expression significantly correlates with monocyte/macrophage markers[29]. Mechanistically, recent studies highlighted S100A8/A9 as a key promoter of myelopoiesis linking fat depots and the BM. While in diabetic mice S100A8/A9 directly induces BM myelopoiesis via RAGE signalling[17], in obesity, monocytosis and neutrophilia are facilitated via S100A8/A9-mediated inflammasome

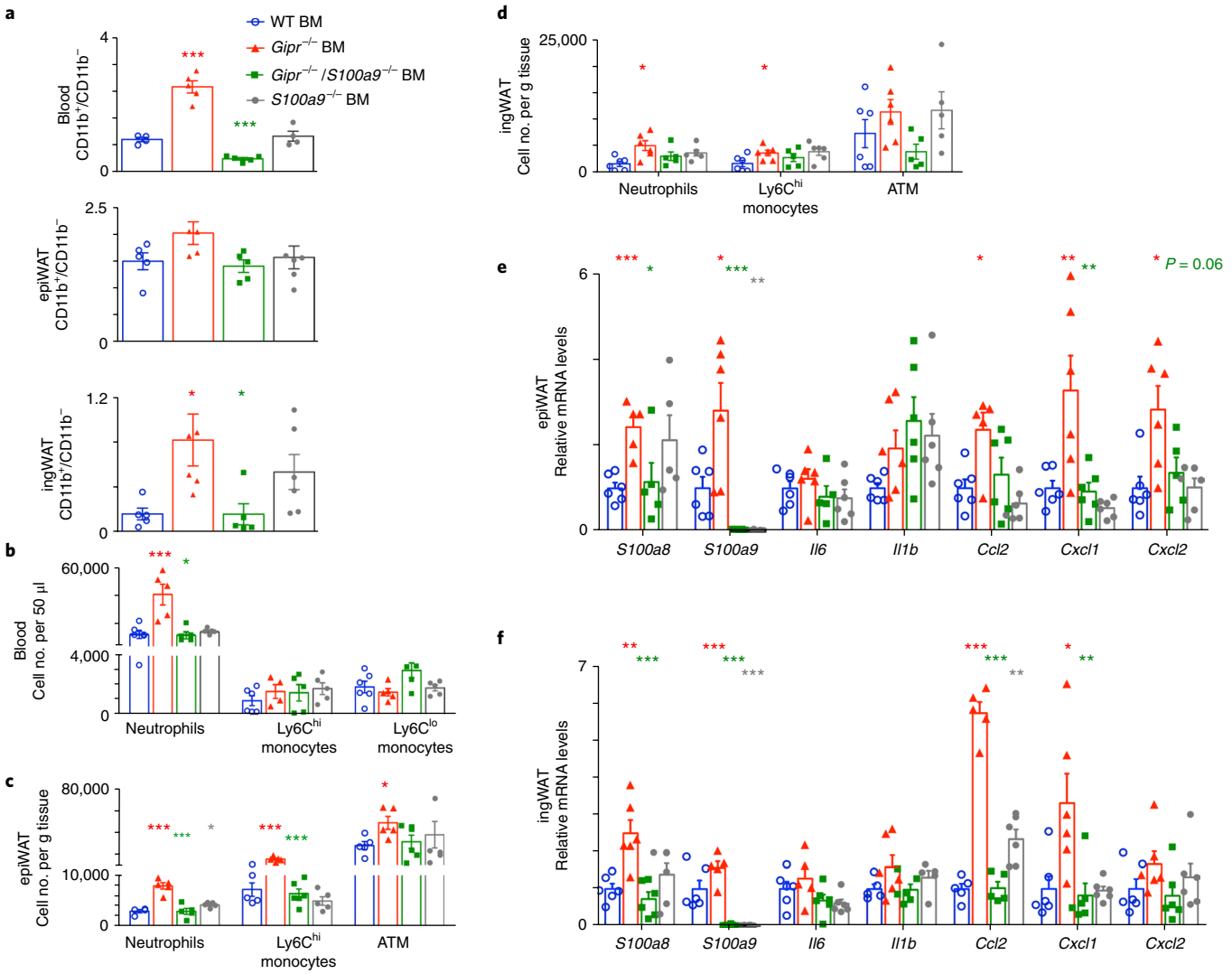

Fig. 5 | Combined deletion of GIPR and S100A8/A9 from immune cells reverses the myelopoiesis phenotype of *Gipr*$^{-/-}$ BM mice. Mice were reconstituted with WT BM (blue open circles), *Gipr*$^{-/-}$ BM (red triangles), *Gipr*$^{-/-}$/*S100a9*$^{-/-}$ BM (green squares) and *S100a9*$^{-/-}$ BM (grey circles) for 6 weeks and then fed a HFD for 14 weeks. **a**, Graphs showing as indication for myelopoiesis the ratio of CD11b^{+} phagocytes versus CD11b^{-} lymphocytes in the blood, epiWAT and ingWAT ($n=6$). **b**–**d**, Bar graphs showing numbers of circulating myeloid cells per 50 µl of blood ($n=6$) (**b**), as well as of neutrophils, Ly6C^{hi} monocytes and ATMs normalized per tissue mass in the epiWAT ($n=6$) (**c**) and ingWAT (**d**) ($n=6$). **e**,**f**, qRT-PCR assessment of the expression of indicated inflammatory mediators normalized to *Rplp0* in epiWAT ($n=6$) (**e**) and ingWAT ($n=6$) (**f**). Data were analysed by one-way ANOVA with Bonferroni. Data are presented as mean ± s.e.m. with significance $^{*}P<0.05$, $^{**}P<0.01$ and $^{***}P<0.001$. Red or grey stars represent significance of *Gipr*$^{-/-}$ BM or *S100a9*$^{-/-}$ BM groups versus WT BM, respectively. Green stars represent significance of *Gipr*$^{-/-}$/*S100a9*$^{-/-}$ BM versus *Gipr*$^{-/-}$ BM. Data are from one experiment.

activation and IL-1β-induced myelopoiesis in the BM[16]. We show that GIPR deletion in immune cells resulted in an S100A8/A9-induced myelopoiesis in blood and in both epiWAT and ingWAT. A main culprit for obesity that developed in HFD-fed *Gipr*$^{-/-}$ BM mice was perturbed heat dissipation, as seen in the metabolic cage experiments and accompanied by impaired beiging in ingWAT. In this respect, we show that S100A8/A9 reduces the expression of UCP1 and PGC1α in ingWAT in a model of cold-induced beiging. Therefore, these results highlight a pathological role for S100A8/A9 in interfering with adaptive thermogenesis, further linking inflammation with metabolic dysfunction.

Given the established deleterious role of S100A8/A9 in obesity-induced inflammation, it seems likely that under physiological conditions of nutrient overload, intact GIPR signalling restrains the deleterious activity of S100A8/A9 originating from immune cells. It might be expected that targeting S100A8/A9 deficiency to immune cells would independently result in an improved metabolic phenotype under HFD conditions. However, we demonstrate quite similar phenotypes in most metabolic and immunologic parameters in WT and *S100a9*$^{-/-}$ BM mice. In these settings, adipocytes seem to be the main source for pathological S100A8/A9[18]. Moreover, phenotypes arising from basal loss of S100A8/A9 in the BM compartment may reflect compensation from multiple mechanisms independently impacting the extent of local inflammation and whole-body energy homeostasis. Hence, further studies are required to further pinpoint the adipocyte versus immune cell-specific roles of S100A8/A9 in energy homeostasis.

It is generally acknowledged that lethal irradiation, as used here in the generation of BM chimeric mice, may limit weight gain. Yet, the augmented weight gain independently observed in the non-irradiated *LysM*$^{\Delta Gipr}$ mice under HFD feeding rules out the importance of irradiation as the major cause for excess weight gain of the *Gipr*$^{-/-}$ BM

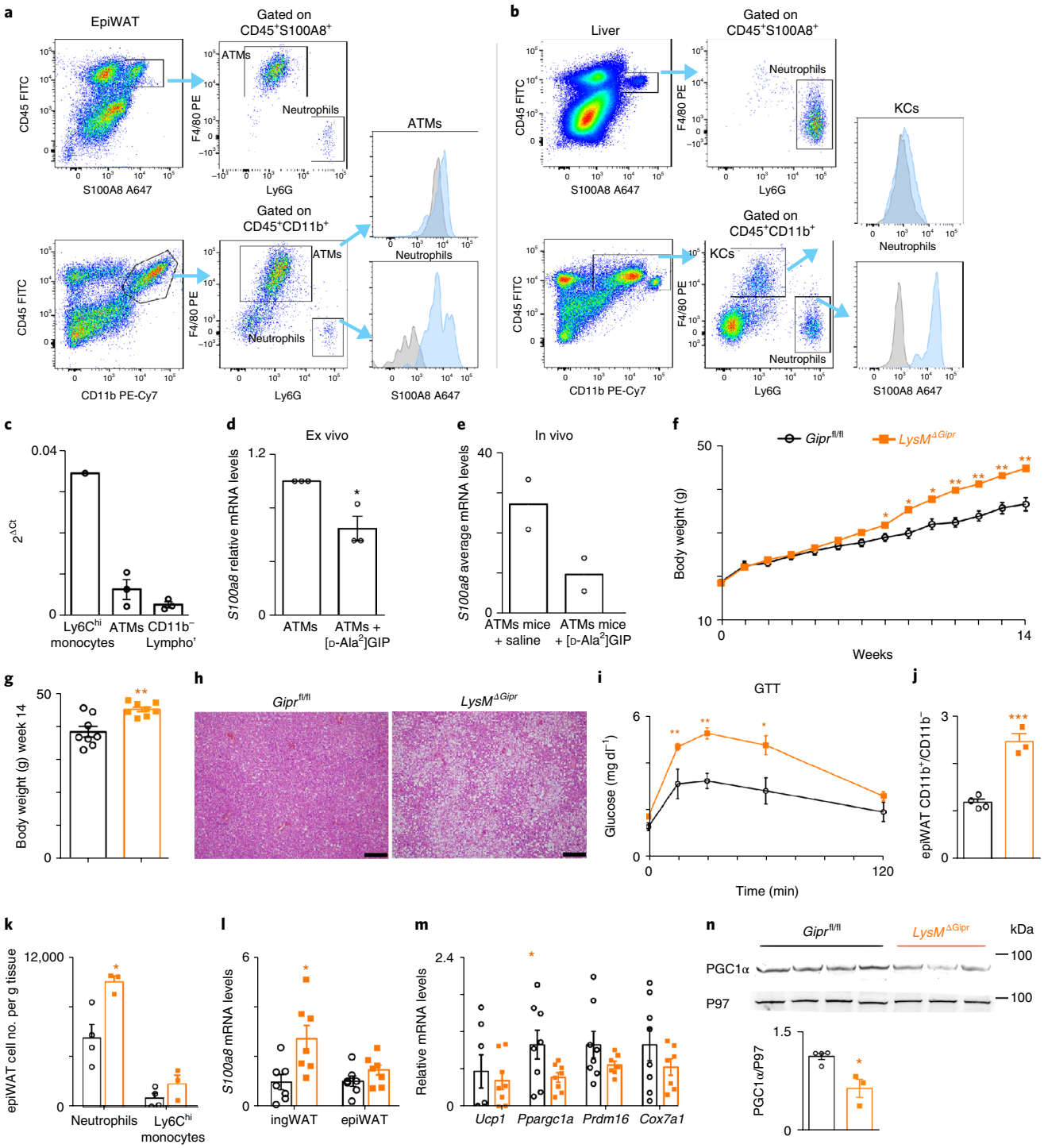

Fig. 6 | GIP negatively regulates S100A8 expression in myeloid cells. a, Flow cytometry of S100A8 in epiWAT ATMs and neutrophils. **b**, Flow cytometry of S100A8 in liver KCs and neutrophils. **c**, *Gipr* mRNA expression in sorted Ly6c^{hi} monocytes ($n=$ pool of 15 mice), ATMs and Cd11b^{-} lymphocytes ($n=3$, each repeat from pool of 5 mice). **d**, qRT-PCR of *S100a8* in ATMs sorted from epiWAT of WT mice after 14 weeks of a HFD and following ex vivo 24 h treatment with 100 nM [D-Ala^2]GIP or vehicle ($n=3$, each repeat from pool of 5 mice, $P=0.017$). **e**, qRT-PCR analysis of *S100a8* expression in ATMs sorted from epiWAT of WT mice after 14 weeks of a HFD and daily intraperitoneal injections of [d-Ala^2]GIP (0.12 µg per g body weight) or vehicle during the last 8 weeks ($n=2$, each repeat from pool of 5 mice). **f**, Body weight of *LysM*$^{\Delta Gipr}$ (orange squares, $n=3$) and littermates *Gipr*$^{fl/fl}$ (black open circles, $n=6$, time point weeks 0–14 $P=0.05$, $P=0.011$, $P=0.013$, $P=0.002$, $P=0.003$, $P=0.004$, $P=0.006$) fed a HFD. **g**, Body weight after 14 weeks of a HFD ($n=8$, $P=0.001$). **h**, Liver H&E paraffin sections. Original magnification, ×10. Scale bars, 200 µm. **i**, GTT of *LysM*$^{\Delta Gipr}$ ($n=5$) and *Gipr*$^{fl/fl}$ ($n=4$, 15 min $P=0.02$, 30 min $P=0.002$, 1 h $P=0.027$). **j**–**k**, Flow cytometry showing myelopoiesis ($P=0.0005$) (**j**) and immune cells in epiWAT ($P=0.021$) (**k**) of *LysM*$^{\Delta Gipr}$ ($n=3$) and *Gipr*$^{fl/fl}$ ($n=5$). **l**, *S100a8* mRNA expression in epiWAT and ingWAT ($n=8$, $P=0.015$). **m**, qRT-PCR of ingWAT thermogenesis genes ($n=8$, for *Ppargc1a* $P=0.04$). **n**, Immunoblot showing PGC1α in ingWAT from *LysM*$^{\Delta Gipr}$ ($n=3$) and *Gipr*$^{fl/fl}$ mice ($n=4$, $P=0.012$), with densitometry presented below. Data was analysed by unpaired, two-tailed *t*-test. Data are presented as mean ± s.e.m with significance $^*P<0.05$ $^{**}P<0.01$ $^{***}P<0.001$. Data in **a**–**d**, **f**, **i**–**k** and **n** are from single experiments, and data in **g**, **l** and **m** are from two experiments.

chimeras. We also provide data showing similar xylose absorption and comparable fat content in the faeces of WT and *Gipr*$^{-/-}$ BM mice under both regular chow and HFD, thus dismissing the possibility that the change in weight gain stems from differences in intestinal nutrient absorption.

Overall, our studies uncover an exciting aspect of GIPR-dependent regulation of energy homeostasis in obesity via myeloid cells and their altered expression of S100A8/A9. Our findings extend our understanding of how sustained food ingestion upregulates hormonal signals from the gut, exemplified by GIP, which in turn provide unique information to different tissues, thereby contributing to control of nutrient-related inflammation and energy homeostasis. Given the new advance in molecular understanding of the sensory machinery by which EECs detect different nutrients, one of the future challenges is to unravel which of the many gut signals is physiologically relevant and might potentially be exploited therapeutically in the treatment of obesity and T2DM. In this respect, GIP multi-agonists are being clinically tested as novel therapeutic agents for T2DM and the metabolic syndrome[11,30,31]. Our data highlight the unexpected role(s) of immune cells as targets for GIP-based therapeutics in the control of inflammation and energy homeostasis.

Methods

Animals. C57BL/6JOlaHsd male mice (Envigo), *Gipr*$^{-/-}$ mice (C57Bl/6 background, provided by Dr Y. Yamada, Akita University, Japan), *S100a9*$^{-/-}$ mice (C57Bl/6 background, provided by Prof. T. Vogl, Munster University, Germany), B6.129P2-*Lyz2*$^{tm1(cre)Ifo}$ (C57Bl/6 background, Jackson Laboratory) and *Gipr*$^{fl/fl}$ mice[24] (C57Bl/6 background, provided by Prof. D. J. Drucker, Mount Sinai Hospital, University of Toronto, Canada) were maintained in specific pathogen-free animal facility, and experiments were performed according to protocols approved by the Animal Care Use Committee of the Sourasky Medical Center. Mice were housed with 12-h light cycles and a constant temperature of 22 °C. For the generation of BM chimeric mice, 6-week-old recipient C57BL/6JOlaHsd male mice were lethally irradiated with 950 rad using a TrueBeam linear accelerator (Varian Medical Systems). The next day, femurs were dissected from 6-week-old donor male mice (WT, *Gipr*$^{-/-}$ and *Gipr*$^{-/-}$/*S100a9*$^{-/-}$ mice). The two ends of the femur were cut and BM cells were flushed out using a 26-G needle containing sterile PBS. After cell counting, 5×10^6 of respective BM cells were injected into the tail vein of the recipients, and mice were allowed to reconstitute their BM-derived immune cells for 6 weeks. After reconstitution, mice were fed with regular chow or a HFD (60% cal from fat, Research Diets, D12492) for 14 weeks.

[D-Ala^2]GIP administration. C57BL/6JOlaHsd male mice (6 weeks old) were fed a HFD for 14 weeks and received a single daily intraperitoneal injection of human [D-Ala^2]GIP (0.12 µg per g body weight) (synthesized by Bio-Synthesis) or vehicle (saline) during the last 8 weeks. Thirty minutes before they were killed, all mice received an intraperitoneal injection of insulin (Actrapid, NovoNordisk) (0.75 U per kg body weight).

Cold exposure. Six-week-old C57BL/6JOlaHsd male mice were intraperitoneally injected with vehicle (saline) or 5 µg S100A8/A9 (R&D Systems) in 200 µl per mouse, then housed in individual cages and exposed to 4 °C in a temperature controlled refrigerator (4–8 °C) for 24 h. The next day, mice were killed, and their ingWAT was assessed for beiging markers by immunohistochemistry and immunoblotting.

Insulin tolerance test. Five days before the end of the experiments, mice were subjected to 6 h of fasting from 7:00 until 13:00, and basal glucose level was determined using the Accu-Check Performa Sensor. Subsequently, insulin (Actrapid) was administered by intraperitoneal injection at a dose of 0.75 U per kg body weight, and serum glucose was measured at indicated time points following the insulin injection.

Glucose tolerance test. One week before the end of the experiments, mice were fasted for 16 h, and then basal glucose was measured using the Accu-Check Performa Sensor. Mice were injected with 2 mg per g body weight glucose, and serum glucose was measured after 15, 30, 60 and 120 min.

Analysis of serum metabolic markers. Mouse serum was collected and kept at −80 °C until assessed. Serum triglycerides were measured using the Advia 2000 Automatic Analyzer. Serum S100A8/A9 levels were measured by enzyme-linked immunosorbent assay (ELISA) in the lab of Prof. T. Vogl using antibodies prepared in his lab. Serum GIP and insulin levels were measured using murine-specific ELISA kits (EMD Millipore), according to the manufacturer's instructions. Basal FFA and FFA after insulin administration were measured using a fluorometric ELISA kit (Abcam).

Metabolic cages. BM chimeric mice fed with a HFD for a total of 8 weeks were individually housed in metabolic chambers with free access to food and water, maintaining a 12 h–12 h dark–light cycle. The LabMaster/PhenoMaster caging systems (TSE Systems) consist of a combination of sensitive feeding and drinking sensors for automated online measurement. Mice were acclimatized in metabolic chambers for 48 h before initiation of data collection. The calorimetry system is an open-circuit system that determines the volume of oxygen consumption (VO_2) and carbon dioxide production (VCO_2), allowing determination of the ratio between fat and glucose utilization for energy. All the parameters were measured continuously and simultaneously for 48 h. Determination of lean and fat mouse mass was performed by using computed tomography (Minispec LF50 Body Composition Analyzer, Bruker).

Determination of D-xylose absorption. After 6 weeks of BM reconstitution, WT BM and *Gipr*$^{-/-}$ BM chimeric mice were fed with a regular chow diet for two weeks. Subsequently, mice were anaesthetized and administered an aqueous solution of 500 µl containing 0.3075 g of D-xylose into the stomach by gavage. After 3 h, mice were bled 1 ml of blood from the orbital plexus. The serum was collected and stored at −80 °C until analysis. Serum was mixed 1:5 with 5% trichloroacetic acid. Samples were centrifuge at 20,817*g*. for 10 min at room temperature. Upper phase was reacted 1:10 with reagent (4 g thiourea, 100 ml glacial acetic acid, 3 g *para*-bromoaniline) and boiled in water bath at 100 °C for 4 min. Optical density at 520 nm was measured using a spectrophotometer.

Determination of fat from faeces. Faeces (100 mg) were collected from WT BM or *Gipr*$^{-/-}$ BM chimeric mice and dried for 1 h at 70 °C and then incubated with 2 ml of chloroform for 30 min at 60 °C and centrifuged 2,000 r.p.m. for 10 min at room temperature. Water was added to the supernatant, and phase separation was induced by low-speed centrifugation at 2,000 r.p.m. for 10 min. The lower chloroform phase was then transferred to a new tube, and the samples were evaporated to dryness and weighed.

Cell isolation procedure from epiWAT, ingWAT and blood. Epididymal fat pads or inguinal subcutaneous fat were surgically removed from mice, weighted, cut into small pieces and subsequently incubated in digestion buffer (DMEM medium, 12.5 mM HEPES buffer pH 7.4, 2% BSA and 10 mg collagenase type II) for 30 min at 37 °C in a shaking bath at 150 r.p.m. The digested tissue was filtered through a 100-µM mesh and centrifuged at room temperature at 500*g* for 5 min. The pellet was washed, and erythrocytes were lysed with red blood cells lysis solution. The SVF was used for flow cytometry analysis. Blood peripheral blood mononuclear and polymorphonuclear cells were isolated using the BD FACS Lysing Solution, according to the manufacturer's instructions.

Flow cytometry analysis and sorting of adipose tissue ATMs. Analysis of myeloid immune cells from SVF and blood was performed according to our previous publication[9]. The antibodies used were against: CD45, CD64, Ly6G, Ly6C, CX3CR1, CD11b, I-A/I-E and F4/80. With respect to S100A8 staining, after surface antigen staining, cells were fixed and permeabilized with BD Cytofix Cytoperm kit and stained intracellularly with an isotype control or S100A8 (provided by Prof. T. Vogl, Munster University, Germany) antibodies, followed by staining with Alex 647 anti-rabbit antibodies. The list of antibodies is presented in Supplementary Table 1. Multi-parameter flow cytometry analyses were performed using the FACSCanto II machine and the FACS DIVA or FlowJo software. Antibodies used are described in the Supplementary Table 1.

Real-time RT–PCR. Total RNA was extracted from isolated livers using TriReagent (Sigma-Aldrich) and from epiWAT, ingWAT and BAT using the QIAzol and Lipid RNA extraction kit (Qiagen). Total RNA was reverse-transcribed using the High Capacity cDNA RT kit (Applied Biosystems). Real-time RT–PCR was performed with the Fast SYBR Green Master Mix (Applied Biosystems) using the Corbett rotor light cycler. Quantification of the PCR signals of each sample was performed by the ΔCt method normalized to *Rplp0* or *Tbp* housekeeping genes. Murine primers used are shown in Supplementary Table 2.

Protein immunoblots. Total protein from liver, epiWAT, ingWAT and BAT was extracted by homogenization in ice-cold RIPA buffer (PBS, 1% Igepal, 0.5% sodium deoxycholate, 0.1% sodium dodecyl sulfate, protease and phosphatase inhibitors cocktails 1:100). Homogenates were centrifuged for 20 min at 14,000*g*, supernatants were collected and extracts were normalized to total protein content. Proteins were separated by SDS–PAGE, blotted onto nitrocellulose and blots were blocked for 1 h in 5% milk. Blots were incubated overnight at 4 °C with antibodies to pAkt (Cell Signaling), Akt1/2, (Santa Cruz Biotechnology), S100A8 (rabbit polyclonal prepared in the lab of Prof. T. Vogl), UCP-1 (Abcam), PGC1α (Abcam) or P97 (rabbit polyclonal prepared in the lab of Prof. Boaz Tirosh, Hebrew University, Jerusalem), and then incubated with horseradish-peroxidase-

conjugated secondary antibody and subjected to chemi-luminescent detection using the Micro Chemiluminescent imaging system (DNR Bio Imaging Systems). Densitometry was performed using the Image J software and expression of p-Akt was normalized to expression of Akt and of the other proteins normalized to expression of housekeeping gene *p97*.

Histological staining and immunohistochemistry for UCP-1. Liver, epiWAT and ingWAT pieces were fixed in 4% paraformaldehyde (EMS) for 24 h and embedded in low melting paraffin (Paraplast Plus, Sigma Aldrich). Five-mm-thick sections were cut (rotary microtome HSM55, Microm) and sections were mounted, dehydrated in increasing ethanol series and stained with H&E (Merck). For UCP-1 immunocytochemistry, slices were subjected to citrate-based antigen retrieval and stained with antibodies to UCP-1 (dilution 1:100, Abcam, ab23841) for 1 h at 4 °C in a humidified chamber. Staining was developed using the VECTASTAIN Elite ABC kit (rabbit immunoglobulin-G) (Vector laboratories, PK-6101), according to the manufacturer's instruction and visualized with a Nikon microscope.

RNA isolation, sample processing and microarray analysis. Total RNA was extracted from epiWAT and ingWAT using the QIAzol Lysis Reagent and Lipid RNA extraction RNeasy Mini Kit (Qiagen), according to the manufacturer's instructions. The isolated RNA was stored at −80 °C. Gene expression profiling was performed using Clariom S arrays (Thermo Fisher Scientific). RNA quantity and quality were determined by measurement of concentration with absorbance at 260 and 280 nm (NanoDrop 2000/2000c spectrophotometers; Thermo, Fisher Scientific) and by TapeStation Analysis (Software A.02.01, Agilent Technologies). Only high-quality RNA with 260/280 nm ratios between 1.9 and 2.1, ratio of 260/230 nm >1.5 and RNA integrity numbers of 6.2–7.9 were used for further microarray analysis. Samples were prepared according to the standard Affymetrix WT PLUS Reagent Kit protocol and Affymetrix WT Terminal Labeling Kit (ThermoFisher) from 100 ng total RNA starting material. GeneChips were washed and stained in the Affymetrix Fluidics Station 450 according to the standard GeneChip Expression Wash, Stain and Scan protocol. Subsequently, the GeneChips were scanned using the Affymetrix 3000 7G scanner. Microarray analysis was performed using Partek Genomics Suite version 6.6 (Partek). Data were normalized and summarized with the robust multiaverage method[34]. Functional enrichment analysis was performed on the differentially expressed genes (≥2-fold change, $P \leq 0.05$, analysis of variance (ANOVA)) using DAVID[32] and WebGestalt[33] tools. Heat maps were generated using Partek Genomics Suite software.

Statistical analysis. Results are presented as means ± s.e.m. Statistical significance between two groups was assessed using a two-tailed Student's *t*-test. Significance was defined if the *P* value was less than 0.05 as follows: $^{*}P<0.05$; $^{**}P<0.01$; $^{***}P<0.001$. Statistical analysis between three groups and above was performed using one-way or two-way ANOVA non-parametric test with Bonferroni correction comparing all pairs of columns. Statistical analyses of gene expression data were performed using the Partek Genomics Suite, DAVID or WebGestalt softwares (ANOVA).

Reporting Summary. Further information on research design is available in the Nature Research Reporting Summary linked to this article.

Data availability

The microarray datasets generated during the current study are deposited at the National Center for Biotechnology Information Gene Expression Omnibus public database under accession code GSE109371.

Received: 7 June 2018; Accepted: 1 October 2018;
Published online: 19 November 2018

References

1. Gribble, F. M. & Reimann, F. Enteroendocrine cells: chemosensors in the intestinal epithelium. *Annu. Rev. Physiol.* **78**, 277–299 (2016).
2. Monteiro, M. P. & Batterham, R. L. The importance of the gastrointestinal tract in controlling food intake and regulating energy balance. *Gastroenterology* **152**, 1707–1717.e2 (2017).
3. Genton, L. & Kudsk, K. A. Interactions between the enteric nervous system and the immune system: role of neuropeptides and nutrition. *Am. J. Surg.* **186**, 253–258 (2003).
4. Brestoff, J. R. & Artis, D. Immune regulation of metabolic homeostasis in health and disease. *Cell* **161**, 146–160 (2015).
5. Miyawaki, K. et al. Inhibition of gastric inhibitory polypeptide signaling prevents obesity. *Nat. Med.* **8**, 738–742 (2002).
6. Kim, S. J., Nian, C. & McIntosh, C. H. Activation of lipoprotein lipase by glucose-dependent insulinotropic polypeptide in adipocytes. A role for a protein kinase B, LKB1, and AMP-activated protein kinase cascade. *J. Biol. Chem.* **282**, 8557–8567 (2007).
7. Gogebakan, O. et al. Glucose-dependent insulinotropic polypeptide reduces fat-specific expression and activity of 11β-hydroxysteroid dehydrogenase type 1 and inhibits release of free fatty acids. *Diabetes* **61**, 292–300 (2012).
8. Kim, S. J. et al. GIP-overexpressing mice demonstrate reduced diet-induced obesity and steatosis, and improved glucose homeostasis. *PLoS ONE* **7**, e40156 (2012).
9. Varol, C. et al. Long-acting glucose-dependent insulinotropic polypeptide ameliorates obesity-induced adipose tissue inflammation. *J. Immunol.* **193**, 4002–4009 (2014).
10. Baggio, L. L. & Drucker, D. J. Biology of incretins: GLP-1 and GIP. *Gastroenterology* **132**, 2131–2157 (2007).
11. Campbell, J. E. & Drucker, D. J. Pharmacology, physiology, and mechanisms of incretin hormone action. *Cell. Metab.* **17**, 819–837 (2013).
12. Pivovarova, O. et al. Regulation of nutrition-associated receptors in blood monocytes of normal weight and obese humans. *Peptides* **65**, 12–19 (2015).
13. Suzuki, Y. et al. Anti-inflammatory role of glucose-dependent insulinotropic polypeptide in periodontitis. *J. Diabetes Investig.* **7**, 497–505 (2016).
14. Nagashima, M. et al. Native incretins prevent the development of atherosclerotic lesions in apolipoprotein E knockout mice. *Diabetologia* **54**, 2649–2659 (2011).
15. Nogi, Y. et al. Glucose-dependent insulinotropic polypeptide prevents the progression of macrophage-driven atherosclerosis in diabetic apolipoprotein E-null mice. *PLoS ONE* **7**, e35683 (2012).
16. Nagareddy, P. R. et al. Adipose tissue macrophages promote myelopoiesis and monocytosis in obesity. *Cell. Metab.* **19**, 821–835 (2014).
17. Nagareddy, P. R. et al. Hyperglycemia promotes myelopoiesis and impairs the resolution of atherosclerosis. *Cell. Metab.* **17**, 695–708 (2013).
18. Sekimoto, R. et al. Visualized macrophage dynamics and significance of S100A8 in obese fat. *Proc. Natl. Acad. Sci. USA* **112**, E2058–E2066 (2015).
19. Harms, M. & Seale, P. Brown and beige fat: development, function and therapeutic potential. *Nat. Med.* **19**, 1252–1263 (2013).
20. Ehrchen, J. M., Sunderkotter, C., Foell, D., Vogl, T. & Roth, J. The endogenous Toll-like receptor 4 agonist S100A8/S100A9 (calprotectin) as innate amplifier of infection, autoimmunity, and cancer. *J. Leukoc. Biol.* **86**, 557–566 (2009).
21. Manitz, M. P. et al. Loss of S100A9 (MRP14) results in reduced interleukin-8-induced CD11b surface expression, a polarized microfilament system, and diminished responsiveness to chemoattractants in vitro. *Mol. Cell. Biol.* **23**, 1034–1043 (2003).
22. Reilly, S. M. & Saltiel, A. R. Adapting to obesity with adipose tissue inflammation. *Nat. Rev. Endocrinol.* **13**, 633–643 (2017).
23. Pruenster, M., Vogl, T., Roth, J. & Sperandio, M. S100A8/A9: from basic science to clinical application. *Pharmacol. Ther.* **167**, 120–131 (2016).
24. Campbell, J. E. et al. TCF1 links GIPR signaling to the control of beta cell function and survival. *Nat. Med.* **22**, 84–90 (2016).
25. Ussher, J. R. et al. Inactivation of the glucose-dependent insulinotropic polypeptide receptor improves outcomes following experimental myocardial infarction. *Cell Metab.* **27**, 450–460 (2018).
26. Foell, D., Wittkowski, H., Vogl, T. & Roth, J. S100 proteins expressed in phagocytes: a novel group of damage-associated molecular pattern molecules. *J. Leukoc. Biol.* **81**, 28–37 (2007).
27. Kim, S. J. et al. A protein profile of visceral adipose tissues linked to early pathogenesis of type 2 diabetes mellitus. *Mol. Cell. Proteomics* **13**, 811–822 (2014)..
28. Mortensen, O. H. et al. Calprotectin—a novel marker of obesity. *PLoS ONE* **4**, e7419 (2009).
29. Catalan, V. et al. Increased levels of calprotectin in obesity are related to macrophage content: impact on inflammation and effect of weight loss. *Mol. Med.* **17**, 1157–1167 (2011).
30. Finan, B. et al. Reappraisal of GIP pharmacology for metabolic diseases. *Trends Mol. Med.* **22**, 359–376 (2016).
31. Frias, J. P. et al. The sustained effects of a dual GIP/GLP-1 receptor agonist, NNC0090-2746, in patients with type 2 diabetes. *Cell. Metab.* **26**, 343–352.E2 (2017).
32. Huang da, W., Sherman, B. T. & Lempicki, R. A. Systematic and integrative analysis of large gene lists using DAVID bioinformatics resources. *Nat. Protoc.* **4**, 44–57 (2009).
33. Wang, J., Vasaikar, S., Shi, Z., Greer, M. & Zhang, B. WebGestalt 2017: a more comprehensive, powerful, flexible and interactive gene set enrichment analysis toolkit. *Nucleic Acids Res.* **45**, 130–137 (2017).
34. Irizarry, R.A., et al. Exploration, normalization, and summaries of high density oligonucleotide array probe level data. *Biostatistics* **4**, 249–264 (2003).

Acknowledgements

The authors acknowledge support from the Israel Science Foundation for C.V. and S.F. (grant nos 35/12 and 1146/16) and the Canada Research Chairs Program and Canadian Institutes of Health Research Foundation grant 154321, both to D.J.D. Y.K. is the incumbent of the Sarah and Rolando Uziel Research Associate Chair. We thank A. H. Futerman and Y. Pewzner-Jung for their assistance with metabolic cages

experiments. Finally, we thank N. Strauss (Sourasky Medical Center) for radiation services.

Author contributions

F.D.M., I.Z., C.V. and S.F. conceived the study, designed experiments and wrote the manuscript. F.D.M., I.Z and C.V. performed the experiments and analysed the data. M.P-C. performed the bioinformatic analyses. T.V. analysed data, provided reagents and reviewed the manuscript. K.C., A.E. and S.W. performed many of the RT–PCR and immunoblot analyses in the presented experiments. Y.K. greatly assisted in the performance of metabolic cages experiments and analyses. D.J.D. provided key scientific consultation, essential reagents and mouse tools and carefully reviewed and edited the manuscript.

Competing interests

The authors declare no competing interests.

Additional information

Supplementary information is available for this paper at https://doi.org/10.1038/s42255-018-0001-z.

Reprints and permissions information is available at www.nature.com/reprints.

Correspondence and requests for materials should be addressed to C.V. or S.F.

Publisher's note: Springer Nature remains neutral with regard to jurisdictional claims in published maps and institutional affiliations.

nature research

Corresponding author(s): Sigal Fishman&Chen Varol
NATMETAB-A18060171B

Reporting Summary

Nature Research wishes to improve the reproducibility of the work that we publish. This form provides structure for consistency and transparency in reporting. For further information on Nature Research policies, see Authors & Referees and the Editorial Policy Checklist.

Statistical parameters

When statistical analyses are reported, confirm that the following items are present in the relevant location (e.g. figure legend, table legend, main text, or Methods section).

n/a	Confirmed	
☐	☒	The exact sample size (*n*) for each experimental group/condition, given as a discrete number and unit of measurement
☐	☒	An indication of whether measurements were taken from distinct samples or whether the same sample was measured repeatedly
☐	☒	The statistical test(s) used AND whether they are one- or two-sided *Only common tests should be described solely by name; describe more complex techniques in the Methods section.*
☐	☒	A description of all covariates tested
☐	☒	A description of any assumptions or corrections, such as tests of normality and adjustment for multiple comparisons
☐	☒	A full description of the statistics including central tendency (e.g. means) or other basic estimates (e.g. regression coefficient) AND variation (e.g. standard deviation) or associated estimates of uncertainty (e.g. confidence intervals)
☒	☐	For null hypothesis testing, the test statistic (e.g. *F*, *t*, *r*) with confidence intervals, effect sizes, degrees of freedom and *P* value noted *Give P values as exact values whenever suitable.*
☒	☐	For Bayesian analysis, information on the choice of priors and Markov chain Monte Carlo settings
☒	☐	For hierarchical and complex designs, identification of the appropriate level for tests and full reporting of outcomes
☒	☐	Estimates of effect sizes (e.g. Cohen's *d*, Pearson's *r*), indicating how they were calculated
☐	☒	Clearly defined error bars *State explicitly what error bars represent (e.g. SD, SE, CI)*

Our web collection on statistics for biologists may be useful.

Software and code

Policy information about availability of computer code

Data collection	*Provide a description of all commercial, open source and custom code used to collect the data in this study, specifying the version used OR state that no software was used.*
Data analysis	Graphpad Prism version 5.0b was used for statistical analysis. BD FACS DIVA (v6.1.3) or FlowJo, LLC v9.9.6 or v10.4.2 were used for flow cytometry analysis. For microarray analyses, RNA quality was measured using the TapeStation Analysis (Software A.02.01, Agilent Technologies). Heatmaps were generated using Partek Genomics Suite version 6.6 (Partek, St. Louis, MO). Pathway enrichment analyses were performed using the bioinformatic tools DAVID and WebGestalt (ref 26, 27). Image J was used to calculate the densitometry of immunoblots.

For manuscripts utilizing custom algorithms or software that are central to the research but not yet described in published literature, software must be made available to editors/reviewers upon request. We strongly encourage code deposition in a community repository (e.g. GitHub). See the Nature Research guidelines for submitting code & software for further information.

Data

Policy information about availability of data

All manuscripts must include a data availability statement. This statement should provide the following information, where applicable:

- Accession codes, unique identifiers, or web links for publicly available datasets
- A list of figures that have associated raw data
- A description of any restrictions on data availability

Reagents for ELISA and immunoblot for S100A8/A9 were uniquely provided by Prof. Thomas Vogl (Munster University, Germany). [D-Ala2]-GIP was synthesized by Bio-Synthesis (Lewisville, Tx). All other reagents are commercially avalilable as indicated in the method section.

Field-specific reporting

Please select the best fit for your research. If you are not sure, read the appropriate sections before making your selection.

☒ Life sciences ☐ Behavioural & social sciences ☐ Ecological, evolutionary & environmental sciences

For a reference copy of the document with all sections, see nature.com/authors/policies/ReportingSummary-flat.pdf

Life sciences study design

All studies must disclose on these points even when the disclosure is negative.

Sample size	Sample size and experiment repeats are clearly indicated in figure legends. The amount of mice used in each of the in vivo experiments was determined in order to meet the requirements of applied measurements and to allow a wide enough representative sample. Sample size was estimated based on our previous experience (see ref 10 for example) as optimal for in-vivo evaluation. For metabolic measurements of body weight, food intake, ITT, serum parameters, and qRT-PCR analyses of metabolic genes all groups contained at least 9 mice and experiments repeated 3 times. Computed tomography calculation of lean and fat mass was as well as metabolic cages analyses in individual caging systems were performed in groups of 5 mice to allow simultaneous observations in these instruments and experiments repeated once. Experiments in cold-exposure challenge included 5 mice per group and repeated twice. Immunological analyses including flow cytometry and qRT-PCR analyses included at least 6 mice per group and repeated twice. For sorting experiments of ATMs, each group contained three repeats, each repeat was extracted from pools of 5 mice. Finally, epiWAT and ingWAT microarray analyses were performed on groups of 3-4 repeats.
Data exclusions	One way or two way ANOVA and unpaired two tailed Student t test were performed using GraphPad Prism (San Diego, CA) and statistical outliers defined by the tests were then excluded from data analysis. Indicated mouse numbers do not include outliers.
Replication	All experiments contain biological replicates as indicated in the legends. Experiments that were repeated on different days showed reproducibility independent of minor day to day variation.
Randomization	Control and experimental groups were initiated at the same age and average body weight.
Blinding	The experiments were not performed with blinding.

Reporting for specific materials, systems and methods

Materials & experimental systems

n/a	Involved in the study
☐	☒ Unique biological materials
☐	☒ Antibodies
☐	☐ Eukaryotic cell lines
☐	☐ Palaeontology
☐	☒ Animals and other organisms
☐	☐ Human research participants

Methods

n/a	Involved in the study
☐	☐ ChIP-seq
☐	☒ Flow cytometry
☐	☐ MRI-based neuroimaging

Unique biological materials

Policy information about availability of materials

Obtaining unique materials

Describe any restrictions on the availability of unique materials OR confirm that all unique materials used are readily available from the authors or from standard commercial sources (and specify these sources).

Antibodies

Antibodies used

Flow cytometry antibodies:

Anti-mouse CD45 FITC Biolegend Cat# 103107 (1:100)

Anti-mouse CD45 APC-Cy7 Antibody Biolegend Cat# 1103116 (1:100)

Anti-mouse F4/80 PE Bio-Rad Cat# MCA497RT (1:50)

Anti-mouse/human CD11b PE-Cy7 Antibody Biolegend Cat# 101216 (1:300)

Anti-mouse Ly6C PerCP/Cy5.5 Antibody Biolegend Cat# 128012 (1:300)

Anti-mouse CD64 APC (FcγRI) Antibody Biolegend Cat# 139306(1: 50)

Anti-mouse Ly6G Brilliant Violet421 Antibody Biolegend Cat# 127628 (1:100)

Anti-Mouse Ly6G FITC Antibody Biolegend Cat# 127606 (1:100)

Anti-mouse CX3CR1 Alexa Fluor® 488 Antibody Biolegend Cat# 149022 (1:100)

Anti-mouse I-A/I-E Pacific Blue Antibody Biolegend Cat# 107620 (1:100)

Rabbit polyclonal anti S100A8 (prof Vogel, house production)(used at concentration of 1ug/ml)

Donkey anti-rabbit Alexa 647 Jackson ImmunoResearch laboratories cat #711-605-152 (1:500)

Immunoblot antibodies:

Rabbit monoclonal anti p-Akt (Ser473) Cell Signaling Cat# 4060(1:1000)

Rabbit polyclonal anti Akt Cell Signaling Cat# 9272 (1:1000)

Rabbit polyclonal anti- S100A8 (MRP8, V/4) (prof. T. Vogl lab. house production)(used at concentration of 1ug/ml)

Rabbit polyclonal anti-PGC1α Abcam cat# ab54481 (1:500)

Rabbit polyclonal anti-UCP1 Abcam cat# ab23841 (1:500)

p97 (rabbit polyclonal prepared in the lab of prof. Boaz Tirosh, Hebrew University, Jerusalem)(1:2000)

Peroxidase conjugated Goat anti-rabbit IgG (Jackson ImmunoResearch laboratories cat #111-035-144 (1:10000)

Validation

Flow cytometry antibodies:

Anti-mouse CD45 FITC Biolegend Cat# 103107 (1:100)

https://www.biolegend.com/en-us/products/fitc-anti-mouse-cd45-antibody-99

Anti-mouse CD45 APC-Cy7 Antibody Biolegend Cat# 1103116 (1:100)
https://www.biolegend.com/en-us/products/apc-cy7-anti-mouse-cd45-antibody-2530

Anti-mouse F4/80 PE Bio-Rad Cat# MCA497RT (1:50)
https://www.bio-rad-antibodies.com/static/datasheets/mca49/mouse-f4-80-antibody-cl-a3-1-mca497rt.pdf

Anti-mouse/human CD11b PE-Cy7 Antibody Biolegend Cat# 101216 (1:300)
https://www.biolegend.com/en-us/products/pe-cy7-anti-mouse-human-cd11b-antibody-1921PE/Cy7 anti-mouse I-Ab Antibody Biolegend Cat# 116420

Anti-mouse Ly6C PerCP/Cy5.5 Antibody Biolegend Cat# 128012 (1:300)
https://www.biolegend.com/en-us/products/percp-cy5-5-anti-mouse-ly-6c-antibody-5967

Anti-mouse CD64 APC (FcγRI) Antibody Biolegend Cat# 139306(1: 50) https://www.biolegend.com/en-us/products/apc-anti-mouse-cd64-fcgammari-antibody-7874

Anti-mouse Ly6G Brilliant Violet421 Antibody Biolegend Cat# 127628 (1:100)
https://www.biolegend.com/en-us/products/brilliant-violet-421-anti-mouse-ly-6g-antibody-7161

Anti-Mouse Ly6G FITC Antibody Biolegend Cat# 127606 (1:100)
https://www.biolegend.com/en-us/products/fitc-anti-mouse-ly-6g-antibody-4775

Anti-mouse CX3CR1 Alexa Fluor® 488 Antibody Biolegend Cat# 149022 (1:100)
https://www.biolegend.com/en-us/products/alexa-fluor-488-anti-mouse-cx3cr1-antibody-11879

Anti-mouse I-A/I-E Pacific Blue Antibody Biolegend Cat# 107620 (1:100)
https://www.biolegend.com/en-us/products/pacific-blue-anti-mouse-i-a-i-e-antibody-3136

Rabbit polyclonal anti S100A8 (prof Vogel, house production)(used at concentration of 1ug/ml)

Donkey anti-rabbit Alexa 647 Jackson ImmunoResearch laboratories cat #711-605-152 (1:500)
https://www.jacksonimmuno.com/catalog/products/711-605-152

Immunoblot antibodies:

Rabbit monoclonal anti p-Akt (Ser473) Cell Signaling Cat# 4060(1:1000)
https://www.cellsignal.com/products/primary-antibodies/phospho-akt-ser473-d9e-xp-rabbit-mab/4060

Rabbit polyclonal anti Akt Cell Signaling Cat# 9272 (1:1000)
https://www.cellsignal.com/products/primary-antibodies/akt-antibody/9272?site-search-type=Products&N=4294956287&Ntt=9272s&fromPage=plp&_requestid=449128
Rabbit polyclonal anti- S100A8 (MRP8, V/4) (prof. T. Vogl lab. house production)(used at concentration of 1ug/ml)

Rabbit polyclonal anti-PGC1α Abcam cat# ab54481 (1:500)
https://www.abcam.com/pgc1-alpha-antibody-ab54481.html

Rabbit polyclonal anti-UCP1 Abcam cat# ab23841 (1:500)
https://www.abcam.com/ucp1-antibody-ab23841.html

p97 (rabbit polyclonal prepared in the lab of prof. Boaz Tirosh, Hebrew University, Jerusalem)(1:2000)

Peroxidase conjugated Goat anti-rabbit IgG (Jackson ImmunoResearch laboratories cat #111-035-144 (1:10000)
www.jacksonimmuno.com/catalog/products/111-035-144

Eukaryotic cell lines

Policy information about cell lines

Cell line source(s)	No eukaryotic cell lines were used
Authentication	No eukaryotic cell lines were used
Mycoplasma contamination	No eukaryotic cell lines were used
Commonly misidentified lines (See ICLAC register)	No eukaryotic cell lines were used

Palaeontology

Specimen provenance

Provide provenance information for specimens and describe permits that were obtained for the work (including the name of the issuing authority, the date of issue, and any identifying information).

Specimen deposition

Indicate where the specimens have been deposited to permit free access by other researchers.

Dating methods

If new dates are provided, describe how they were obtained (e.g. collection, storage, sample pretreatment and measurement), where they were obtained (i.e. lab name), the calibration program and the protocol for quality assurance OR state that no new dates are provided.

☐ Tick this box to confirm that the raw and calibrated dates are available in the paper or in Supplementary Information.

Animals and other organisms

Policy information about studies involving animals; ARRIVE guidelines recommended for reporting animal research

Laboratory animals

C57BL/6JOlaHsd male mice (Envigo, Jerusalem), Gipr-/- mice (provided by Dr Y. Yamada, Akita University, Japan), S100a9-/- mice (on C57Bl/6 background, provided by Prof. T. Vogl, Munster University, Germany) were used fto generate bone marrow chimeras.
Gipr fl/fl (on C57Bl/6 background, provided by Prof.D Drucker,Toronto) and LysM cre (B6.129P2-Lyz2tm1(cre)Ifo/J from Jackson laboratories) were used for generate Lysm -cre. Gipr fl/fl mice. All mice were maintained in specific pathogen-free animal facility and experiments were performed according to protocols approved by the Animal Care Use Committee of the Sourasky Medical Center. Mice were housed with 12 hr light cycles and a constant temperature of 22°C.

Wild animals

Provide details on animals observed in or captured in the field; report species, sex and age where possible. Describe how animals were caught and transported and what happened to captive animals after the study (if killed, explain why and describe method; if released, say where and when) OR state that the study did not involve wild animals.

Field-collected samples

For laboratory work with field-collected samples, describe all relevant parameters such as housing, maintenance, temperature, photoperiod and end-of-experiment protocol OR state that the study did not involve samples collected from the field.

Human research participants

Policy information about studies involving human research participants

Population characteristics

Describe the covariate-relevant population characteristics of the human research participants (e.g. age, gender, genotypic information, past and current diagnosis and treatment categories). If you filled out the behavioural & social sciences study design questions and have nothing to add here, write "See above."

Recruitment

Describe how participants were recruited. Outline any potential self-selection bias or other biases that may be present and how these are likely to impact results.

ChIP-seq

Data deposition

☐ Confirm that both raw and final processed data have been deposited in a public database such as GEO.

☐ Confirm that you have deposited or provided access to graph files (e.g. BED files) for the called peaks.

Data access links
May remain private before publication.

For "Initial submission" or "Revised version" documents, provide reviewer access links. For your "Final submission" document, provide a link to the deposited data.

Files in database submission

Provide a list of all files available in the database submission.

Genome browser session
(e.g. UCSC)

Provide a link to an anonymized genome browser session for "Initial submission" and "Revised version" documents only, to enable peer review. Write "no longer applicable" for "Final submission" documents.

Methodology

Replicates

Describe the experimental replicates, specifying number, type and replicate agreement.

Sequencing depth

Describe the sequencing depth for each experiment, providing the total number of reads, uniquely mapped reads, length of reads and whether they were paired- or single-end.

Antibodies

Describe the antibodies used for the ChIP-seq experiments; as applicable, provide supplier name, catalog number, clone name, and lot number.

Peak calling parameters	*Specify the command line program and parameters used for read mapping and peak calling, including the ChIP, control and index files used.*
Data quality	*Describe the methods used to ensure data quality in full detail, including how many peaks are at FDR 5% and above 5-fold enrichment.*
Software	*Describe the software used to collect and analyze the ChIP-seq data. For custom code that has been deposited into a community repository, provide accession details.*

Flow Cytometry

Plots

Confirm that:

☒ The axis labels state the marker and fluorochrome used (e.g. CD4-FITC).

☒ The axis scales are clearly visible. Include numbers along axes only for bottom left plot of group (a 'group' is an analysis of identical markers).

☒ All plots are contour plots with outliers or pseudocolor plots.

☒ A numerical value for number of cells or percentage (with statistics) is provided.

Methodology

Sample preparation	Epididymal fat pads or inguinal subcutaneous fat stromal vascular fractions (SVF) - fat pads were surgically removed from mice, weighted, cut into small pieces and subsequently incubated in digestion buffer [DMEM, 12.5 mM HEPES pH 7.4, 2% BSA and 10mg collagenase type II] for 30 min at 37 degrees C in a shaking bath at 150 rpm. The digested tissue was filtered through a 100µM mesh and centrifuged at room temperature at 500Xg for 5 min. The pellet was washed and erythrocytes were lysed with red blood cells lysis solution. Blood peripheral blood mononuclear and polymorphonuclear cells were isolated using the BD FACS(TM) Lysing Solution, according to manufacturer's instructions. Cells from SVF and blood were stained according to the manufacturer orders using the listed antibodies and dilutions. With respect to S100A8 staining, after surface antigen staining, cells were fixed and permeabilized with BD Cytofix Cytoperm kit and stained intracellularly with an isotype control or S100A8 (provided by Prof. T. Vogl, Munster University, Germany) antibodies, followed by staining with Alex 647 anti-rabbit antibodies.
Instrument	FACSCanto™ II machine(BD Biosciences, USA)
Software	Data were analyzed using BD FACS DIVA (v6.1.3) or FlowJo (LLC, v9.9.6 or v10.4.2) softwares
Cell population abundance	EpiWAT ATMs, Ly6Chi monocytes or CD11b(neg) lymphocytes were sorted to high purity using the cell sorter BD FACSAria™ III machine (BD Biosciences, USA). For all populations, purity was above 90% as calculated out of total living cells.
Gating strategy	Blood monocytes: CD45+CD11b+CD115+Ly6G- monocytes were dissected into Ly6Chi and Ly6Clo subsets Blood neutrophils: CD45+CD11b+CD115-Ly6Ghi EpiWAT or IngWAT ATMs: CD45+CD11b+MHCII+CD64+F4/80+ EpiWAT or IngWAT neutrophils: CD45+CD11b+MHCII-CD64-/loF4/80-/loLy6Ghi EpiWAT or IngWAT Ly6Chi monocytes: CD45+CD11b+MHCII-CD64loF4/80lo Ly6G-Ly6Chi All gating strategies are exemplified at Figure 2 and Supplementary Figure 8.

☒ Tick this box to confirm that a figure exemplifying the gating strategy is provided in the Supplementary Information.

Magnetic resonance imaging

Experimental design

Design type	*Indicate task or resting state; event-related or block design.*
Design specifications	*Specify the number of blocks, trials or experimental units per session and/or subject, and specify the length of each trial or block (if trials are blocked) and interval between trials.*
Behavioral performance measures	*State number and/or type of variables recorded (e.g. correct button press, response time) and what statistics were used to establish that the subjects were performing the task as expected (e.g. mean, range, and/or standard deviation across subjects).*

Acquisition

Imaging type(s) — *Specify: functional, structural, diffusion, perfusion.*

Field strength — *Specify in Tesla*

Sequence & imaging parameters — *Specify the pulse sequence type (gradient echo, spin echo, etc.), imaging type (EPI, spiral, etc.), field of view, matrix size, slice thickness, orientation and TE/TR/flip angle.*

Area of acquisition — *State whether a whole brain scan was used OR define the area of acquisition, describing how the region was determined.*

Diffusion MRI ☐ Used ☐ Not used

Preprocessing

Preprocessing software — *Provide detail on software version and revision number and on specific parameters (model/functions, brain extraction, segmentation, smoothing kernel size, etc.).*

Normalization — *If data were normalized/standardized, describe the approach(es): specify linear or non-linear and define image types used for transformation OR indicate that data were not normalized and explain rationale for lack of normalization.*

Normalization template — *Describe the template used for normalization/transformation, specifying subject space or group standardized space (e.g. original Talairach, MNI305, ICBM152) OR indicate that the data were not normalized.*

Noise and artifact removal — *Describe your procedure(s) for artifact and structured noise removal, specifying motion parameters, tissue signals and physiological signals (heart rate, respiration).*

Volume censoring — *Define your software and/or method and criteria for volume censoring, and state the extent of such censoring.*

Statistical modeling & inference

Model type and settings — *Specify type (mass univariate, multivariate, RSA, predictive, etc.) and describe essential details of the model at the first and second levels (e.g. fixed, random or mixed effects; drift or auto-correlation).*

Effect(s) tested — *Define precise effect in terms of the task or stimulus conditions instead of psychological concepts and indicate whether ANOVA or factorial designs were used.*

Specify type of analysis: ☐ Whole brain ☐ ROI-based ☐ Both

Statistic type for inference (See Eklund et al. 2016) — *Specify voxel-wise or cluster-wise and report all relevant parameters for cluster-wise methods.*

Correction — *Describe the type of correction and how it is obtained for multiple comparisons (e.g. FWE, FDR, permutation or Monte Carlo).*

Models & analysis

n/a	Involved in the study
☐	☐ Functional and/or effective connectivity
☐	☐ Graph analysis
☐	☐ Multivariate modeling or predictive analysis

Functional and/or effective connectivity — *Report the measures of dependence used and the model details (e.g. Pearson correlation, partial correlation, mutual information).*

Graph analysis — *Report the dependent variable and connectivity measure, specifying weighted graph or binarized graph, subject- or group-level, and the global and/or node summaries used (e.g. clustering coefficient, efficiency, etc.).*

Multivariate modeling and predictive analysis — *Specify independent variables, features extraction and dimension reduction, model, training and evaluation metrics.*

nature metabolism

SUPPLEMENTARY INFORMATION

https://doi.org/10.1038/s42255-018-0001-z

In the format provided by the authors and unedited.

GIP regulates inflammation and body weight by restraining myeloid-cell-derived S100A8/A9

Fernanda Dana Mantelmacher[1,7], Isabel Zvibel[1,7], Keren Cohen[1], Alona Epshtein[1], Metsada Pasmanik-Chor[2], Thomas Vogl[3], Yael Kuperman[4], Shai Weiss[1], Daniel J. Drucker[5], Chen Varol[1,6]* and Sigal Fishman[1]*

[1]The Research Center for Digestive Tract and Liver Diseases, Tel-Aviv Sourasky Medical Center and the Sackler School of Medicine, Tel-Aviv University, Tel-Aviv, Israel. [2]Bioinformatics Unit, Faculty of Life Science, Tel Aviv University, Tel-Aviv, Israel. [3]Institute of Immunology, University of Münster, Münster, Germany. [4]Department of Veterinary Resources, Weizmann Institute of Science, Rehovot, Israel. [5]The Lunenfeld-Tanenbaum Research Institute, Mount Sinai Hospital, University of Toronto, Toronto, Ontario, Canada. [6]Department of Clinical Microbiology and Immunology, Sackler School of Medicine, Tel-Aviv University, Tel-Aviv, Israel. [7]These authors contributed equally: Fernanda Dana Mantelmacher, Isabel Zvibel. *e-mail: chenv@tlvmc.gov.il; sigalf@tlvmc.gov.il

Supplementary information

Supplementary figures

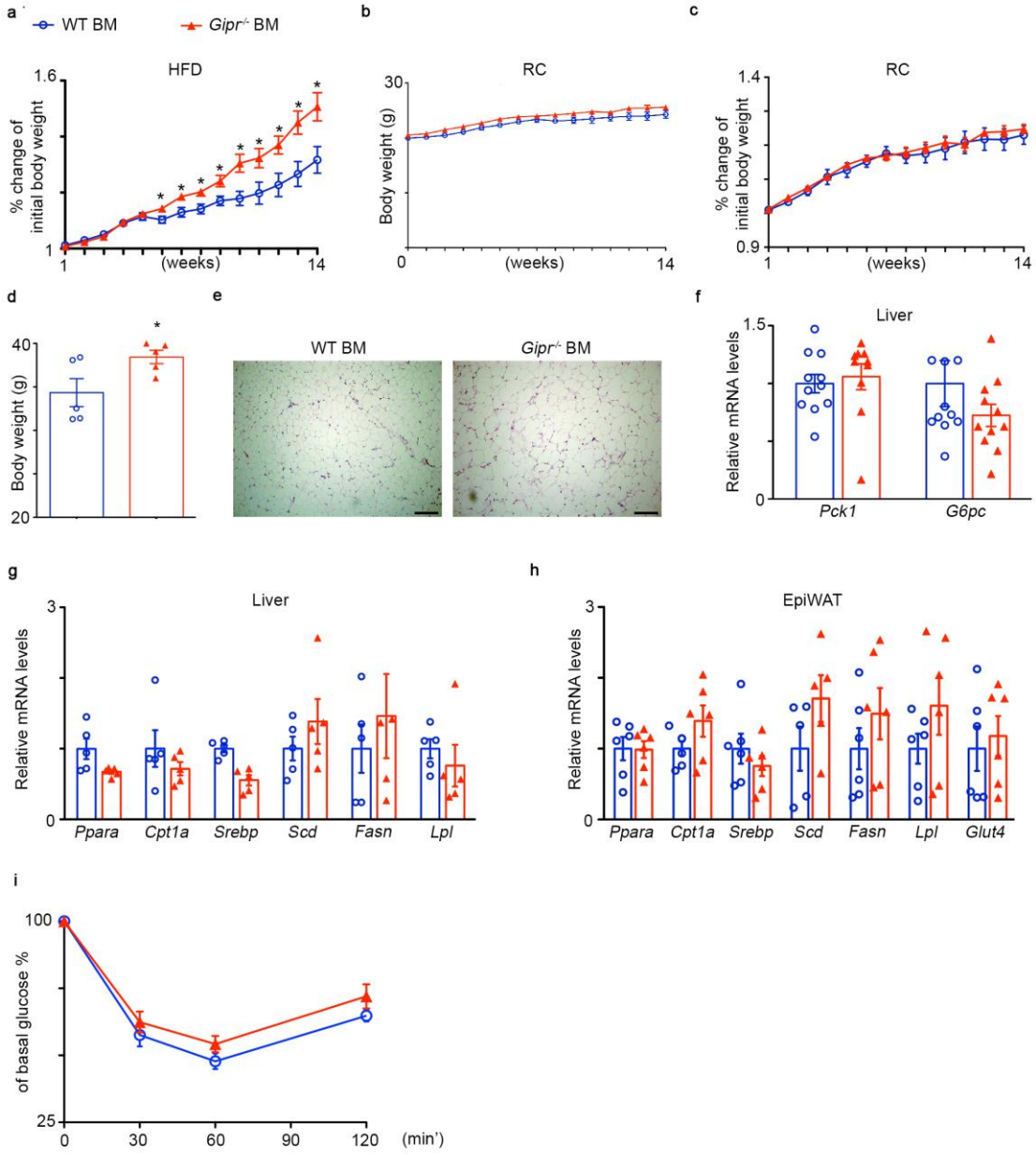

Supplementary Figure 1: Metabolic parameters in WT and *Gipr*$^{-/-}$ BM mice.

Mice were reconstituted with WT BM (blue open circles) or *Gipr*$^{-/-}$ BM (red triangles) for 6 weeks and then fed with RC or HFD for 14 weeks or 18 weeks. (**a**) Percentage of weight gain (%) from initial weight in WT BM (blue open circles) or *Gipr*$^{-/-}$ BM fed HFD for 14 weeks (n=10, time point week 6-14 p=0.013, P=0.014, P=0.014, P=0.015,

P=0.01, P=0.04, P=0.03, P=0.016, P=0.022) (**b**) Body weight gain of mice under RC (g) (n=5 each group). (**c**) Body weight gain under RC (%) (n=5 each group) (**d**) Final body weight of mice reconstituted with WT BM or *Gipr*$^{-/-}$ BM after 18 weeks HFD (g) (n=5, P=0.051). (**e**) Representative H&E sections of ingWAT of mice reconstituted with WT BM or *Gipr*$^{-/-}$ BM Original magnification x10. Bars, 200 μm. (**f**) Hepatic expression of gluconeogenesis genes after 14 weeks HFD was determined by qRT-PCR and normalized to *Rplp0* (n=11). (**g**) Hepatic expression of lipogenesis and β-oxidation genes after 14 weeks HFD was determined by qRT-PCR and normalized to *Rplp0* (n=5 each group). (**h**) Expression of metabolic genes after 14 weeks HFD was assessed in epiWAT and normalized to *Rplp0* (n=6 each group). (i) ITT showing % of basal glucose in WT BM and *Gipr*$^{-/-}$ BM mice from Fig.1h (WT BM mice n=6, *Gipr-/-* BM mice n=5). Data were analyzed by unpaired, two-tailed *t*-test, comparing each time between WT BM and *Gipr*$^{-/-}$ BM mice, and are presented as mean ± SEM. Data in a-b are from single experiments and in d-f from two separate experiments.

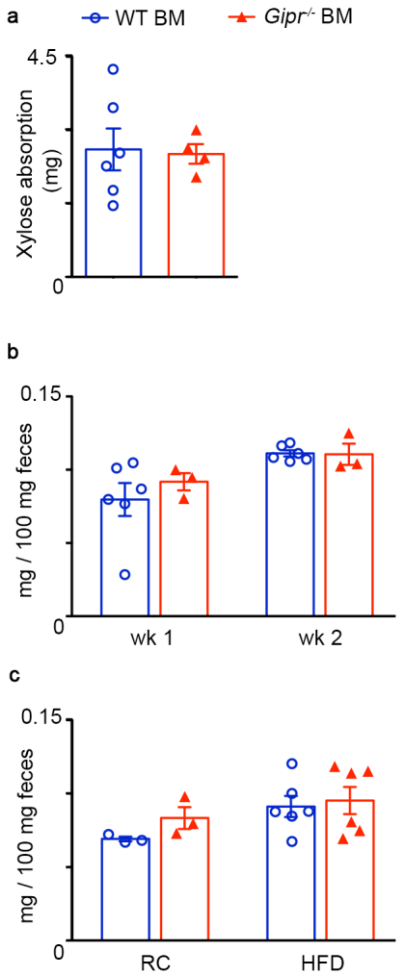

Supplementary Figure 2: *Gipr*$^{-/-}$ BM mice do not have impaired intestinal absorption either during the bone marrow reconstitution phase or during the HFD feeding period. Mice were reconstituted with WT BM (blue open circles) or *Gipr*$^{-/-}$ BM (red triangles) for 6 weeks and then fed RC or HFD. (**a**) Six weeks after BM reconstitution and 2 weeks following RC feeding, a xylose absorption test was performed in the chimeric mice. Graph shows similar absorption in both groups (n=6 for WT BM mice, n=4 for *Gipr*$^{-/-}$ BM mice). (**b**) Fat content in feces was measured under RC at one week (n=5 for WT BM mice, n=3 for Gipr-/- BM mice) and two weeks (n=6 for WT BM mice, n=3 for *Gipr*$^{-/-}$ BM mice) during the reconstitution period, as well as after five weeks of HFD (n=3 each group) or RC (n=6 each group)

(**c**). Data were analyzed by unpaired, two-tailed *t*-test, comparing each time between WT BM and *Gipr*$^{-/-}$ BM mice, and are presented as mean ± SEM.

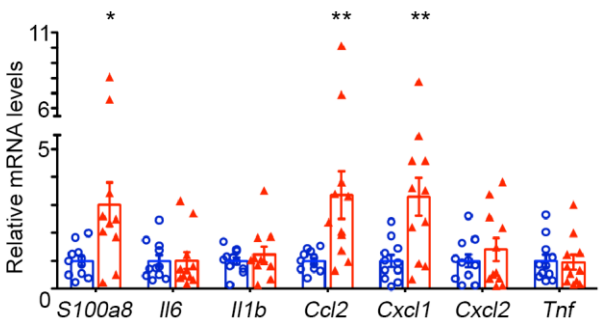

Supplementary Figure 3: Hepatic expression of inflammatory mediators. The expression of inflammatory cytokines and chemokines genes after 14 weeks of HFD was determined by qRT-PCR and normalized to *Rplp0* (n=11 each group, for *S100a8* p=0.016, for *Ccl2* p=0.012, for *Cxcl1* p=0.004). Data were analyzed by unpaired, two-tailed *t*-test, comparing between WT BM and *Gipr*$^{-/-}$ BM mice and the results are presented as mean ± SEM.

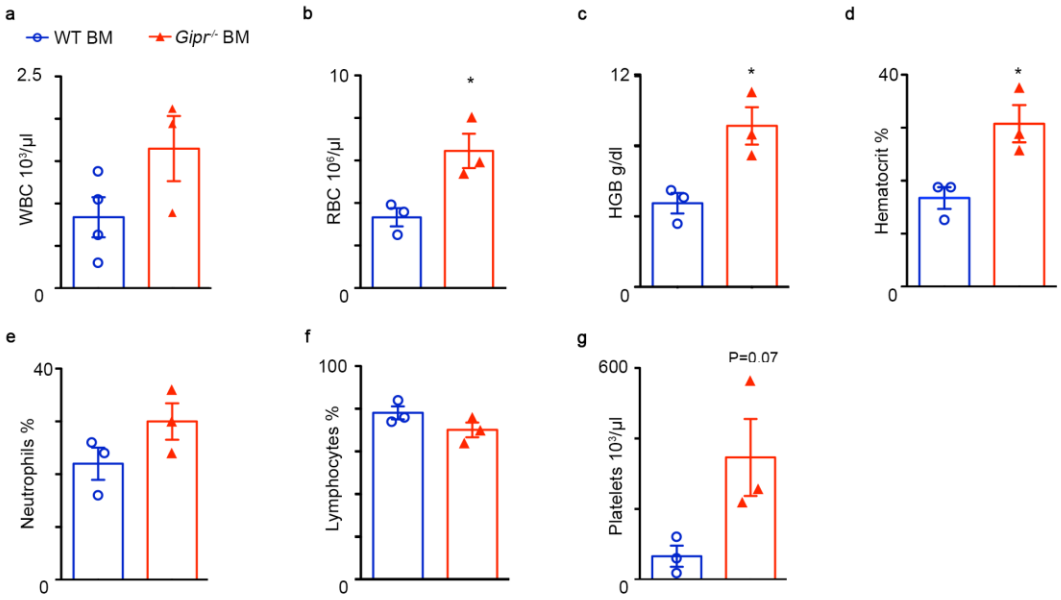

Supplementary Figure 4: Blood count of WT BM versus *Gipr*$^{-/-}$ BM mice on HFD. Mice were reconstituted with WT BM (blue open circles, n=4 mice) or *Gipr*$^{-/-}$ BM (red triangles, n=3 mice) for 6 weeks and then fed HFD for 14 weeks. (a) White blood cell (WBC) count (ul). (b) Red blood cell (RBC) count (ul) (p=0.027). (c) Hemoglobin (HGB) count (dl) (p=0.022). (d) Hematocrit (p=0.026) (e) % Neutrophils and (f) Lymphocytes % from serum. (g) Platelets (p=0.068) (ul). Data were analyzed by unpaired, two-tailed *t*-test, comparing between WT BM and *Gipr*$^{-/-}$ BM mice and the results are presented as mean ± SEM. Data are from a single experiment.

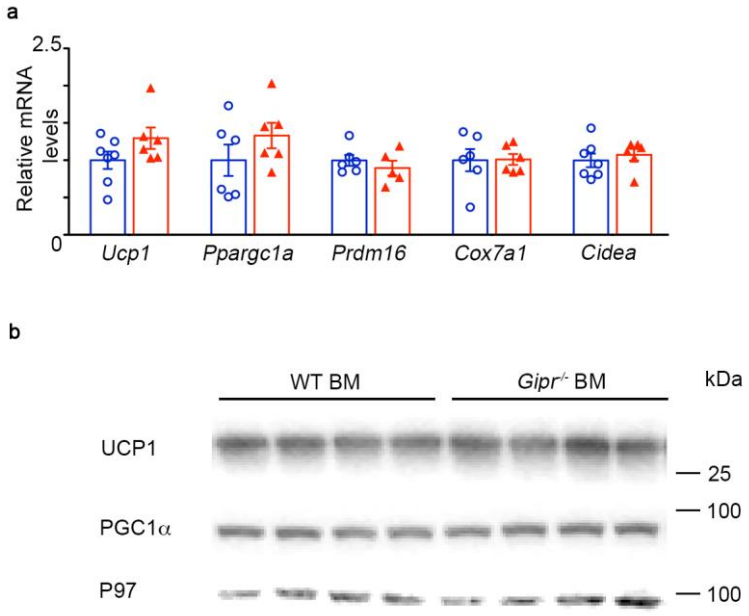

Supplementary Figure 5: Molecular markers of thermogenesis in brown adipose tissue (BAT).

Mice were reconstituted with WT BM (blue open circles) or *Gipr*$^{-/-}$ BM (red triangles) for 6 weeks and then fed HFD for 14 weeks. (**a**) Expression of BAT thermogenesis genes was assessed by qRT-PCR and normalized to *Rplp0* (WT BM n=7, *Gipr*$^{-/-}$ BM n=6). (**b**) Representative immunoblots of thermogenesis proteins UCP1 and PGC1α in BAT demonstrating similar expression of the proteins in the two groups of mice. P97 was used as control (n=4 each group). Data were analyzed by unpaired, two-tailed *t*-test, comparing between WT BM and *Gipr*$^{-/-}$ BM mice, and are presented as mean ± SEM. Data represent two independent experiments.

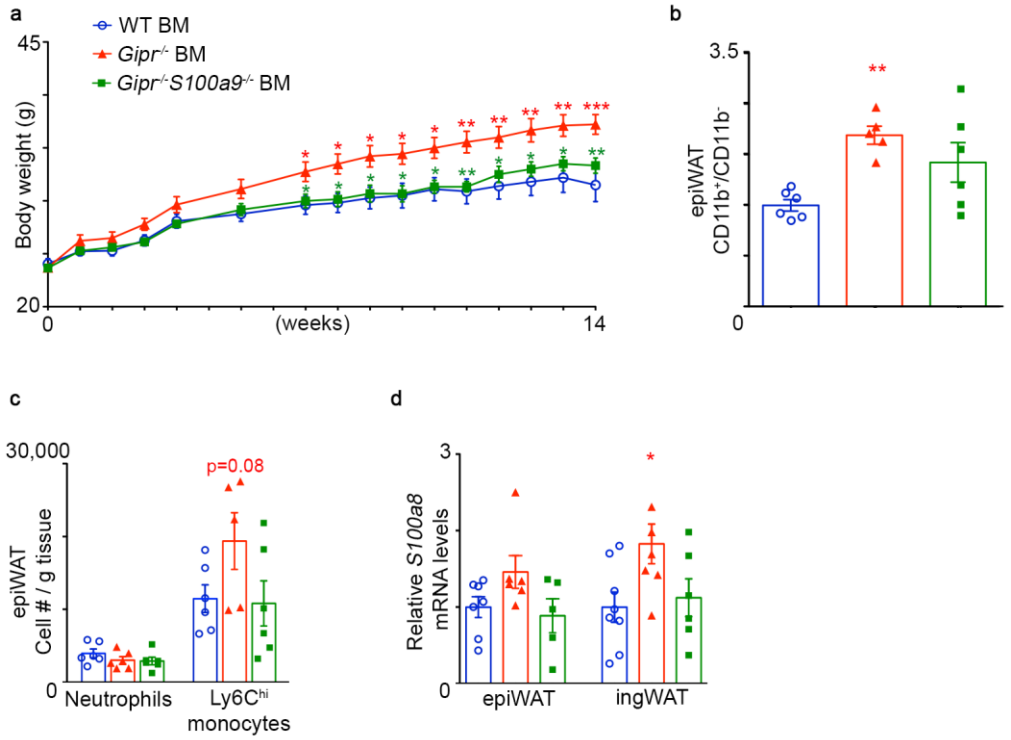

Supplementary Figure 6: Double deletion of GIPR and S100A8/A9 from immune cells reverses the metabolic and myelopoiesis phenotypes displayed by *Gipr*$^{-/-}$ BM mice also at 18 weeks of HFD. Mice were reconstituted with WT BM (blue open circles), *Gipr*$^{-/-}$ BM (red triangles) and *Gipr*$^{-/-}$*/S100a9*$^{-/-}$ BM (green squares) for 6 weeks and then fed with HFD for 18 weeks. (**a**) Weekly measurements of body weight (n=6). (**b**) Graphs showing as indication for myelopoiesis the ratio of CD11b^{+} phagocytes vs. CD11b^{-} lymphocytes in the epiWAT (n=6). (**c**) Bar graphs showing numbers of neutrophils and Ly6C^{hi} monocytes normalized per tissue mass in the epiWAT (n=6). (**d**) qRT-PCR assessment of *S100a8* expression normalized to *Rplp0* in the ingWAT and epiWAT (WT BM mice n=10, *Gipr*$^{-/-}$ BM mice n=10, *Gipr*$^{-/-}$*/S100a9*$^{-/-}$ BM mice n=8). Data were analyzed by one way ANOVA with Bonferroni and are presented as mean ± SEM with significance: *p<0.05 **p<0.01 ***p<0.001. Red stars represent significance of *Gipr*$^{-/-}$ BM group vs. WT BM. Green stars

represent significance of *Gipr*$^{-/-}$/*S100a9*$^{-/-}$ BM vs. *Gipr*$^{-/-}$ BM. Data are from a single experiment.

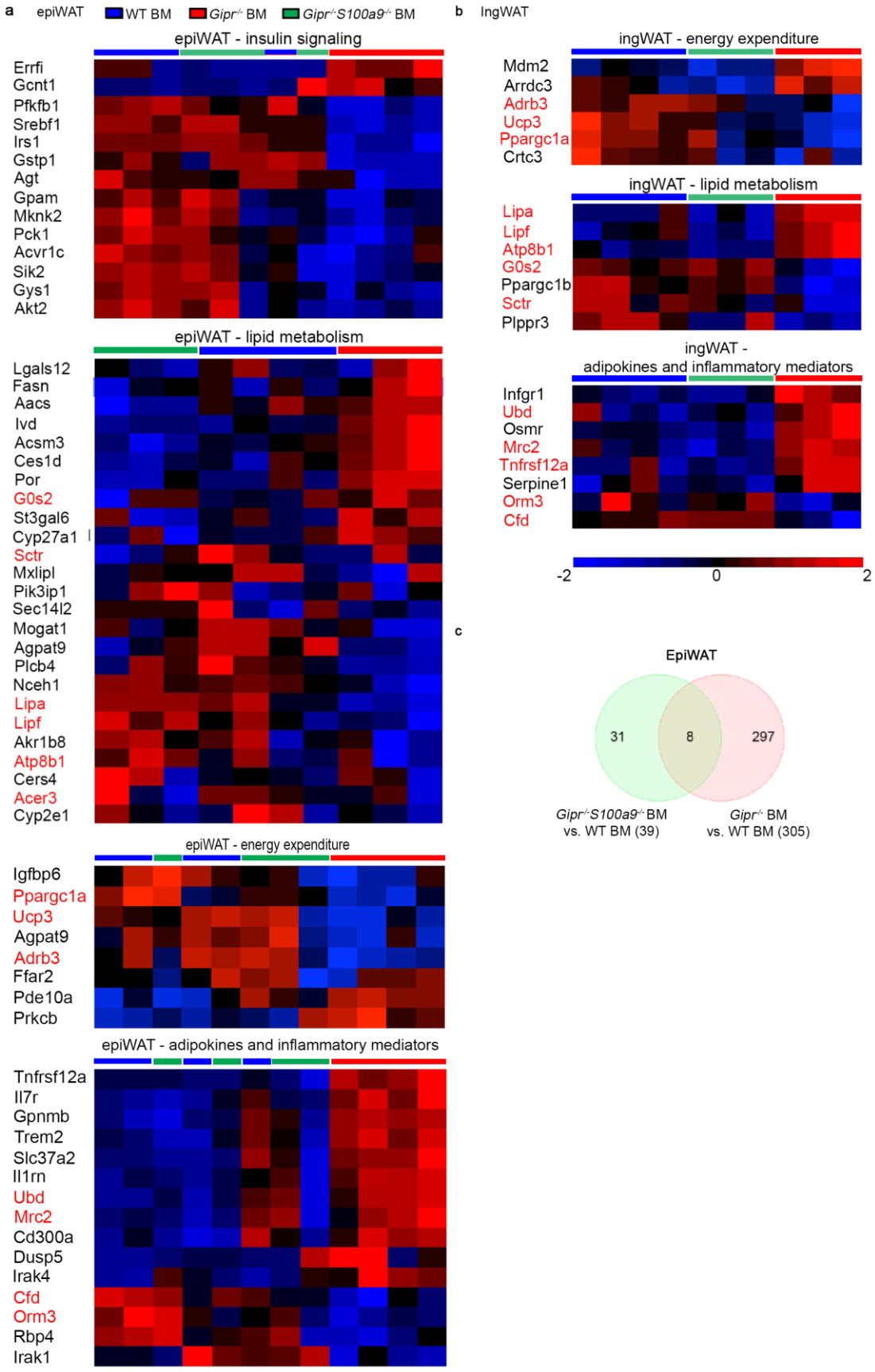

Supplementary Figure 7: Double deletion of GIPR and S100A8/A9 from immune

cells reverses the gene expression alterations observed in epiWAT and ingWAT of *Gipr*$^{-/-}$ BM mice.

Mice were reconstituted with WT BM (blue), *Gipr*$^{-/-}$ BM (red) and *Gipr*$^{-/-}$*/S100a9*$^{-/-}$ BM (green) for 6 weeks and then fed with HFD for 14 weeks. Subsequently, mRNA was extracted from epiWAT and ingWAT and subjected to Affymetrix gene array. Differentially expressed genes were obtained using a cut off of at least 2-fold change (p value <0.05). Venn diagram showing the distribution of 336 genes (epiWAT) and of 1455 genes with above 2-fold expression difference in the comparison between *Gipr*$^{-/-}$*S100a9*$^{-/-}$ BM vs. WT BM and *Gipr*$^{-/-}$ BM vs. WT BM. (**a**) Heatmaps visualizing the hierarchical clustering of differentially expressed genes (Fold-change ≥2, p<0.05, ANOVA) that are associated with pathways in epiWAT: insulin signaling, lipid metabolism, energy expenditure and adipokines and inflammatory mediators (n≥3). (**b**) Heatmaps visualizing the hierarchical clustering of differentially expressed genes (Fold-change ≥2, p<0.05, ANOVA) that are associated with pathways in ingWAT: energy expenditure, lipid metabolism and adipokines and inflammatory mediators (n≥3). Genes that are altered in both epiWAT and ingWAT are marked with red color. Data are from a single experiment. (**c**) Venn diagram showing the distribution of 336 genes with above 2-fold expression difference in the comparison between epiWATs of *Gipr*$^{-/-}$*S100a9*$^{-/-}$ BM vs. WT BM and *Gipr*$^{-/-}$ BM vs. WT BM.

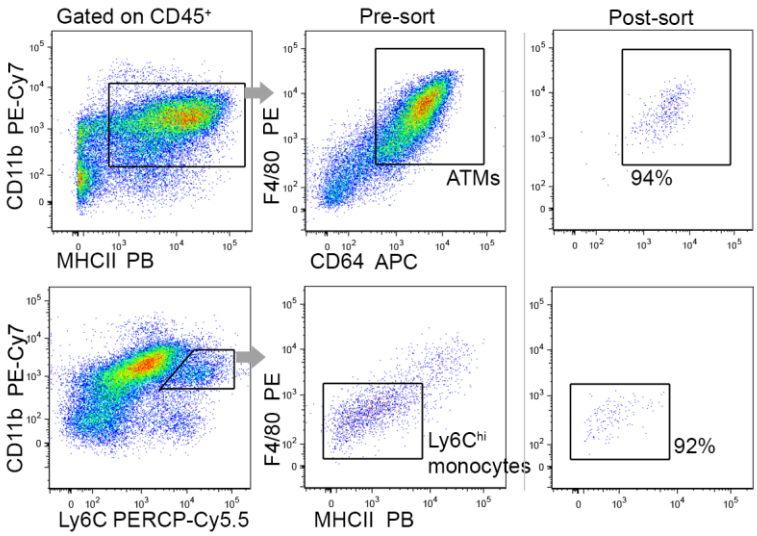

Supplementary Figure 8: Gating strategy used to sort Ly6c^{hi} monocytes and ATM from epiWAT of mice fed HFD for 14 weeks. Left panel, flow cytometry images showing the gating strategy used for the sorting of Ly6c^{hi} monocytes (n=15 mice) and ATMs (n=5, three repetitions) from epiWAT of WT mice fed with HFD for 14 weeks. Right panel, flow cytometry images showing sorting purity for each of the indicated populations.

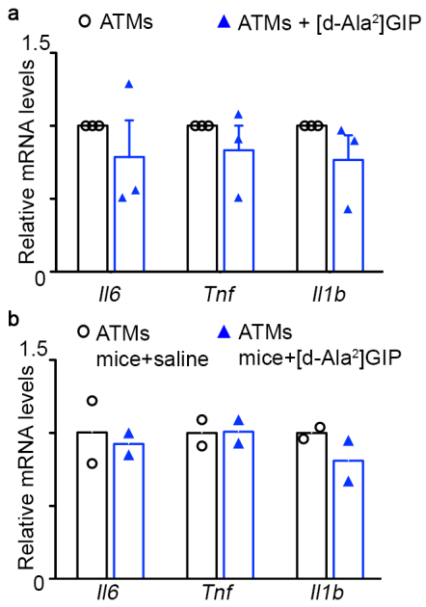

Supplementary Figure 9: GIP treatment does not affect the gene expression of other inflammatory cytokines in sorted ATMs. Expression of inflammatory cytokines analyzed by qRT-PCR and normalized to *Tbp* in (**a**) ATMs sorted from epiWAT of WT mice after 14 weeks of HFD and following *ex vivo* 24 h treatment with 100nM d[Ala2]-GIP or vehicle ($PBS^{-/-}$). Cytokine expression is presented as fold induction versus untreated controls. (n= 3, each repeat represents a pool of 5 mice). (**b**) Expression of inflammatory cytokines analyzed by qRT-PCR and normalized to *Tbp* in sorted ATMs from epiWAT of WT mice after 14 weeks of HFD and daily i.p injections of d[Ala2]-GIP (0.12μg/g body weight) or vehicle ($PBS^{-/-}$) during the last eight weeks (n= 2, each repeat represents a pool of 5 mice).

Figure 1m

pAKT

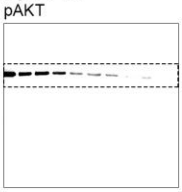

AKT

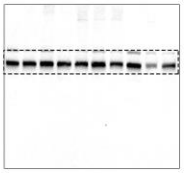

Figure 1n

pAKT

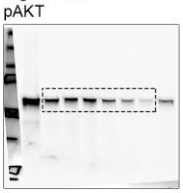

AKT

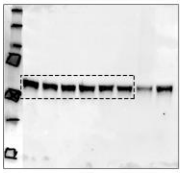

Figure 2b

S100A8

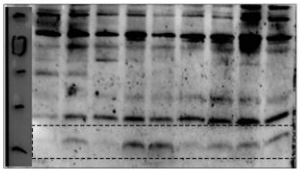

P97

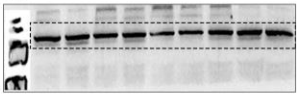

Figure 3e

UCP1

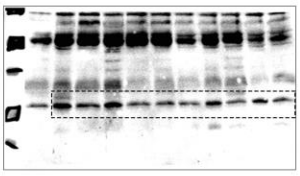

P97

Figure 3g

PGC1α

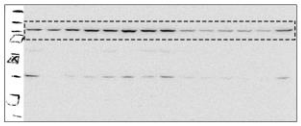

UCP1

P97

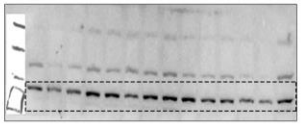

P97

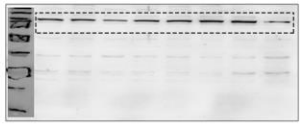

Figure 6n

PGC1

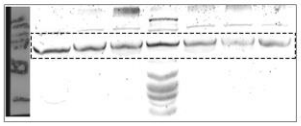

P97

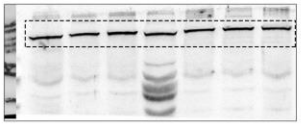

Supplementary Figure 10: Original Western blots

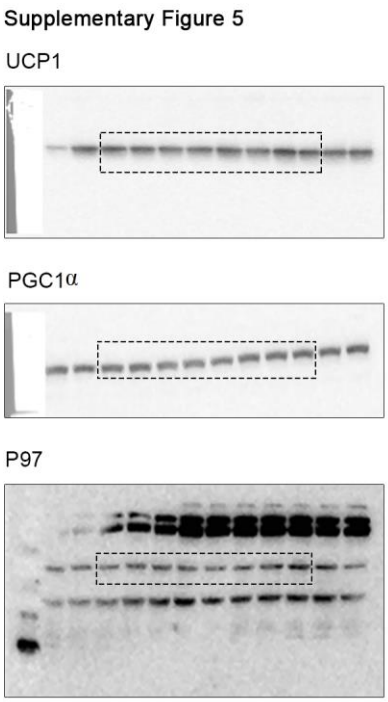

Supplementary Figure 11: Original Western blots of supplementary Figure 5.

Supplementary Table 1: Antibodies used for flow cytometry

Antibody	**Source**	**Catalog number**
APC anti-mouse CD64 (FcγRI) Antibody	Biolegend	Cat# 139306
APC/Cy7 anti-mouse CD45 Antibody	Biolegend	Cat# 103116
Brilliant Violet421 anti-mouse Ly6G Antibody	Biolegend	Cat# 127628
Pacific Blue anti-mouse I-A/I-E Antibody	Biolegend	Cat# 107620
PerCP/Cy5.5 anti-mouse Ly6C Antibody	Biolegend	Cat# 128012
PE anti-mouse CD115 (CSF-1R) Antibody	Biolegend	Cat# 135506
PE/Cy7 anti-mouse/human CD11b Antibody	Biolegend	Cat# 101216
PE rat anti-mouse F4/80 Antibody	Bio-Rad	Cat# MCA497RT
Alexa 647 anti- rabbit antibody	Jackson	Cat#711605152

Supplementary Table 2: Sequences of murine oligonucleotide primers for qRT-PCR

Gene	**Left primer**	**Right primer**
Sterol regulatory element-binding protein-1 (*Srebp)*	GCGCTACCGGTCTTCTATCA	TGTGCACTTCGTAGGGTCAG
Fatty acid synthase (*Fasn*)	ATTGTCGCTCTGAGGCTGTT	GCTGGCTGATACAGAGAGCA
Stearoyl-Coenzyme A desaturase-1 (*Scd*)	TGCGATACACTCTGGTGCTC	TAGTCGAAGGGGAAGGTGTG
Lipoprotein lipase (*Lpl*)	GGGCTCTGCCTGAGTTGTAG	CCACCTCAGTCCCAGAAAA
Peroxisome proliferator	ATGCCAGTACTGCCG	TTGCCCAGAGATTTG

activated receptor alpha (*Ppara*)	TTTTC	AGGTC
Carnitine palmitoyltransferase (*Cpt1a*)	CATGTCAAGCCAGACGAAGA	CTTTCGACCCGAGAAGACCT
Glucose transporter type 4 (*Glut4*)	AGCGAGTGACTGGAACACTG	AGAGCCCAGAGCGTAGTGAG
Calcium-binding protein A8 (*S100a8*)	GGAAATCACCATGCCCTCTA	TGGCTGTCTTTGTGAGATGC
Calcium-binding protein A9 (*S100a9*)	GAAGGAAGGACACCCTGACA	TCAACTTTGCCATCAGCATC
Interleukin 6 (*Il6*)	CCGGAGAGGAGACTTCACAG	TTCTGCAAGTGCATCATCGT
Interleukin 1β (*Il1b*)	GACCTTCCAGGATGAGGACA	AGCTCATATGGGTCCGACAG
Chemokine (C-C motif) ligand 2 (*Ccl2*)	AGGTCCCTGTCATGCTTCTG	GCTGCTGGTGATCCTCTTGT
Chemokine (C-X-C motif) ligand 1 (*Cxcl1*)	CTTGAAGGTGTTGCCCTCAG	TCTGAACCAAGGGAGCTTCA
Chemokine (C-X-C motif) ligand 2 (*Cxcl2*)	AGTGAACTGCGCTGTCAATG	TTCAGGGTCAAGGCAAACTT
Thermogenin Uncoupling protein 1 (*Ucp1*)	CTTCTCAGCCGGAGTTTCAG	GGCAATCCTTCTGTTTTTGC
Peroxisome proliferator-activated receptor gamma coactivator 1-alpha	AATGCAGCGGTCTTAGCACT	GTGTGAGGAGGGTCATCGTT

(*Ppargc1a*)		
PR domain containing 16 (*Prdm16*)	GATCTTCCCCAGATCTGCAA	ACGGCTTCTCTTTGTTGTGG
Cytochrome c oxidase polypeptide 7A1 (*Cox7a1*)	AAAACCGTGTGGCAGAGAAG	CAGCGTCATGGTCAGTCTGT
Cell death activator CIDE-A (*Cidea*)	TGGAAAAGGGACAGAAATGG	TCTCGTACATCGTGGCTTTG
Glucose-dependent insulinotropic polypeptide receptor (*Gipr*)	GTGTCTTGCCCCTGGTATCT	AGCCCCATTCTTCTCTGGAT
CD137 Tumor necrosis factor receptor superfamily, member 9 (*Tnfrsf9*)	GCCCTCCAAGTACCTTCTCC	GCCTGCAGTCCTTTTCACAT
β adrenergic receptor 3 (*Adrb3*)	ACAGGAATGCCACTCCAATC	TTAGCCACAACGAACACTCG
Thermogenin Uncoupling protein 3 (*Ucp3*)	ATGAGTTTTGCCTCCATTCG	GGCGTATCATGGCTTGAAAT
Transcription factor A, mitochondrial *(Tfam)*	CCGAAGTGTTTTTCCAGCAT	GGCTGCAATTTTCCTAACCA
Nuclear respiratory factor 1 *(Nrf1)*	AAAGCTGCAAGCCTATCTGG	GGTGGCCTGAGTTTGTGTTT
Cytochrome oxidase subunit 4i1*(Cox4i1)*	ACCGCATCCAGTTTAACGAG	CCCAGTCACGATCGAAAGTA

T-box1 *(Tbx*)	CGACAAGCTGAAAC TGACCA	GTGACTGCAGTGAA GCGTGT
Acidic ribosomal protein P0*(Rplp0*)	CAACCCAGCTCTGG AGAAAC	GTTCTGAGCTGGCAC AGTGA
TATA box binding protein (*Tbp)*	CCCCACAACTCTTCC ATTCT	CAGCCAAGATTCAC GGTAGA